Laser-Induced Incandescence Measurements of Soot Production in Steady and Flickering Methane, Propane, and Ethylene Diffusion Flames

CHRISTOPHER R. SHADDIX* and KERMIT C. SMYTH†

Building and Fire Research Laboratory, National Institute of Standards and Technology, Gaithersburg, MD 20899

Quantitative experimental measurements of soot concentrations and soot scattering are presented for a series of steady and flickering coflowing methane, propane, and ethylene flames burning at atmospheric pressure. Flickering diffusion flames exhibit a wide range of time-dependent, vortex-flame sheet interactions, and thus they serve as an important testing ground for assessing the applicability of chemical models derived from steady flames. Acoustic forcing of the fuel flow rate is used to phase lock the periodic flame flicker close to the natural flame flicker frequency caused by buoyancy-induced instabilities. For conditions in which flame clip-off occurs, the peak soot concentrations in the methane flickering flames are 5.5 to 6 times larger than measured in a steady flame burning with the same mean fuel flow rate, whereas the enhancement for the flickering propane and ethylene flames is only 35 to 60%, independent of the flicker intensity. Soot concentration profiles and full Mie analysis of the soot volume fraction/scattering results reveal significant differences in the structure of the soot fields and in the roles of soot inception, growth, and oxidation for the different hydrocarbon fuels.

The soot concentrations have been measured using laser-induced incandescence (LII). Since this is the only technique currently available for making time- and spatially-resolved soot concentration measurements in time-varying flow fields, considerable effort has been devoted to developing LII for quantitative applications. Important considerations include (1) proper calibration measurements, (2) signal detection which minimizes interferences from C_2 Swan-band emission and broadband molecular fluorescence, (3) correction for the laser beam focus/spatial averaging effect in line image measurements, and (4) correction for LII signal extinction within the flame.

1. INTRODUCTION

The study of periodic, time-varying laminar diffusion flames provides the opportunity for critical evaluation of both qualitative and quantitative insights gained from investigations of simpler, steady laminar flames. Time-varying flames exhibit a broader range of stoichiometry, strain rate, and temperature histories than are commonly found in steady flames, which makes their examination particularly valuable in extending ideas and relationships developed from steady flames to the analysis of more practical, but more difficult to interpret, turbulent conditions. Flickering flames are generally defined as those observed (e.g., by luminosity) to undergo large-scale, low-frequency oscillations, where the oscillation frequency is related to the flame diameter by $f[\mathrm{Hz}] \approx 1.5/(D[m])^{1/2}$ [1, 2]. Such behavior often occurs in diffusion flames, whether originating from gaseous jets, liquid pools, or solid combustibles, due to the formation and convection of strong vortex rings on the outside of the main flame zone. These large vortical structures likely arise from a modified type of Kelvin-Helmholtz hydrodynamic instability due to the shear between the buoyant, high-temperature gases and the cooler, slowly moving surrounding air [3–5]. Little is known about the effect of periodic oscillations and the accompanying vortex structures on the chemical and thermal fields *within* the flame or on emissions *from* the flame. For example, the slow rates of aromatic hydrocarbon formation and soot inception and growth, which render the concentrations of aromatics and soot independent of the mixture fraction [6–10], might be expected to result in strong sensitivity of these quantities to the flow-field dynamics present in

* National Research Council NIST Postdoctoral Research Associate, 1993–1995; present address: Combustion Research Facility, Sandia National Laboratories, Livermore, CA 94551.

†Corresponding author.

0010-2180/96/$15.00
PII S0010-2180(96)00107-1

time-varying flames. Variations in soot concentrations can, in turn, significantly affect the emitted radiation. Furthermore, the slow rates of carbon monoxide (CO) oxidation and soot burnout and their strong dependence on the local temperature [11, 12] may be expected to result in striking effects on the emission of these toxic compounds from time-varying flames.

In an earlier study of OH· laser-induced fluorescence and elastic scattering from soot in steady and time-varying methane/air flames, the UV soot scattering intensity was found to be much greater in the flickering flames (by a factor of 10 to 20) than that observed for the corresponding steady flame with the same mean fuel and air flow rates [13]. Measurements of the soot volume fraction fields in the steady and a moderately flickering flame using both laser extinction and calibrated laser-induced incandescence (LII) techniques revealed a factor of 5 enhancement in the peak soot volume fraction, and a factor of 4 increase in the time-averaged, volume-integrated soot volume fraction in the flickering flame [14]. The LII results showed superior signal-to-noise with respect to the extinction data, particularly in the time-varying flame (due to flame wobble effects and the need to average the extinction measurements over a number of flame cycles). These were the first spatially and temporally resolved quantitative soot volume fraction results to be reported in a time-varying flow field.

Mie analysis of the LII and vertically polarized UV scattering measurements suggested that soot particle number densities in the flickering methane/air flame are comparable to steady flame values ($\approx 2\text{–}3 \times 10^9/\text{cm}^3$ in the middle of the soot layer, assuming a monodisperse size distribution), whereas optical particle sizes increase from a maximum of 60 nm in the steady flame to $\approx$ 90 nm in the moderately flickering flame. Furthermore, in a recent collaborative effort [15] the two-dimensional, time-dependent, reactive-flow Navier–Stokes equations were coupled with submodules for soot formation [16] and radiation transport and were solved for both steady and time-varying CH_4/air diffusion flames. These simulations successfully predict the observed soot concentrations in both the steady and flickering flames. Analysis of the time history of the fluid parcels which pass through the maximum soot volume fraction shows that the time-varying flames exhibit longer residence times during which the local temperatures and stoichiometries are favorable for soot production. This extension of the soot growth residence time is predicted to increase with increasing flicker intensity.

The present study extends these previous quantitative measurements of soot production in steady and flickering methane/air flames to propane/air and ethylene/air systems. These fuels (along with methane/air) are of interest because they form the bulk of prior detailed studies on soot formation in laminar diffusion flames [e.g., 9, 17–19]. Furthermore, since diffusion flame soot chemistry is highly sensitive to fuel type [20] and methane is the most weakly sooting hydrocarbon fuel, the trends in soot production observed for the flickering methane flames cannot be assumed to hold for other hydrocarbon fuels. The effect of flicker intensity on the soot field is also investigated here by analyzing flames produced by two different characteristic forcing amplitudes.

These measurements for three hydrocarbon fuels burning under both steady and flickering conditions constitute an extensive database for comparison with the predictions of integrated soot models. In particular, the results of Moss et al. [9, 16, 21, 22], Kennedy et al. [23–25], Lindstedt et al. [26, 27], and Kent et al. [28–30] for the rates of soot inception, growth, and oxidation can now be tested in combusting flow fields more complex than the steady flames on which these models are based. This is the prime objective of our comparison [15] of measured soot concentrations in steady and flickering methane flames with the soot model of Moss et al. [16].

The present paper also includes a detailed description of our laser-induced incandescence measurement technique. The LII method can potentially provide quantitative soot concentrations in a single laser shot at a point, along a line, or for a 2-D image. This development is especially exciting for interrogation of complex, time-varying flow fields. However, various conflicting approaches have been advocated in the literature, and our experience indicates

that significant corrections which have not been previously implemented are often required for accurate results.

2. EXPERIMENTAL METHODS

Our previous Rayleigh-limit and full Mie analysis of the optical soot measurements in methane flames [14] was restricted by the short wavelength radiation (283.5 nm) used to obtain the scattering data and the resultant large particle size parameters ($x = \pi D/\lambda$, where D is the particle diameter), particularly in the upper regions of the flickering flame. Since soot particles are composed of clusters of aggregated primary particles, neither a Rayleigh-limit nor full Mie analysis may be expected to be accurate for overall particle sizes outside of the Rayleigh regime (defined as $x \ll 1$) [31]. Full Mie theory results are presented here, since there is evidence that they are superior to a Rayleigh-limit description for both the mean volume equivalent diameters and particle number densities when compared with the more accurate fractal agglomerate analysis [32]. In order to broaden the applicability of the Mie analysis, particularly for the more strongly sooting propane and ethylene flames, 560.3-nm laser light was used for the present scattering experiments. In addition, the LII experiments have been improved over our previous measurements [14] in several ways: (1) selection of a detection bandpass to reduce contributions from laser-induced C_2 Swan-band emission, which does not necessarily scale with the soot volume fraction and can also arise from molecular sources; (2) correction for the laser beam focus/spatial averaging effect in line-image measurements; and (3) correction for LII signal extinction in the flame, which becomes quite significant for the propane and ethylene fuels. The soot scattering signals have also been corrected for both extinction of the incident laser beam and extinction of the scattering signal itself within the flame.

2.1. Burner and Imaging Set-Up

Unconfined laminar diffusion flames were stabilized on a coannular burner with a 10.2-cm-diameter air annulus surrounding a 1.1-cm-diameter fuel tube, with a loudspeaker attached to the plenum below the fuel tube. As with previous studies [13, 14], the optical diagnostics were phase locked to a sinusoidal oscillation of the fuel stream at the 10-Hz repetition rate of a Nd^{3+}: YAG laser, permitting phase-specific measurements to be performed in the time-varying flow fields. Figure 1 shows a schematic diagram of the burner and phase-locked imaging set-up. In contrast to our prior experiments, a synthesized function generator has replaced both a variable delay pulse generator and a signal generator to provide exact reproducibility of the flickering flame forcing amplitude and the detection phase settings. Images were recorded at 90° to the propagation direction of the laser beam using an intensified charge-coupled device (ICCD) camera. An $f/4.5$, 100-mm focal length UV lens was mounted on the camera for these measurements and was focused on the burner centerline for 3.8 : 1 imaging.

The air coflow was 635 cm^3/s for the methane flames and 685 cm^3/s for the propane and ethylene flames. Mean fuel flow rates were approximately normalized to the methane flame fuel flow rate (7.5 cm^3/s) on a carbon atom basis, giving visible flame heights of $\approx$ 85 mm and 91 mm for the propane/air and ethylene/air steady flames, respectively, compared to 79 mm for the methane/air flame. The cold flow area-averaged fuel/air velocities are listed in Table 1. OH· concentrations have been measured previously in this steady CH_4 flame and in a slightly shorter (4.0 cm/s, termed Non-Smoking, or NS) C_2H_4 flame [33], and soot properties have been extensively measured for the NS C_2H_4 flame [18, 34–36]. Our measurements were performed on the three different steady flames and on both moderately and strongly flickering flames produced by applying sine waves of magnitude 0.75 V and 1.5 V (peak-to-peak voltage) to the plenum loudspeaker.

2.2. Visible Light Scattering

Vertically polarized dye laser light at 560.3 nm was expanded into a vertical sheet using a single spherical lens and two cylindrical lenses. The lens combination resulted in a laser sheet

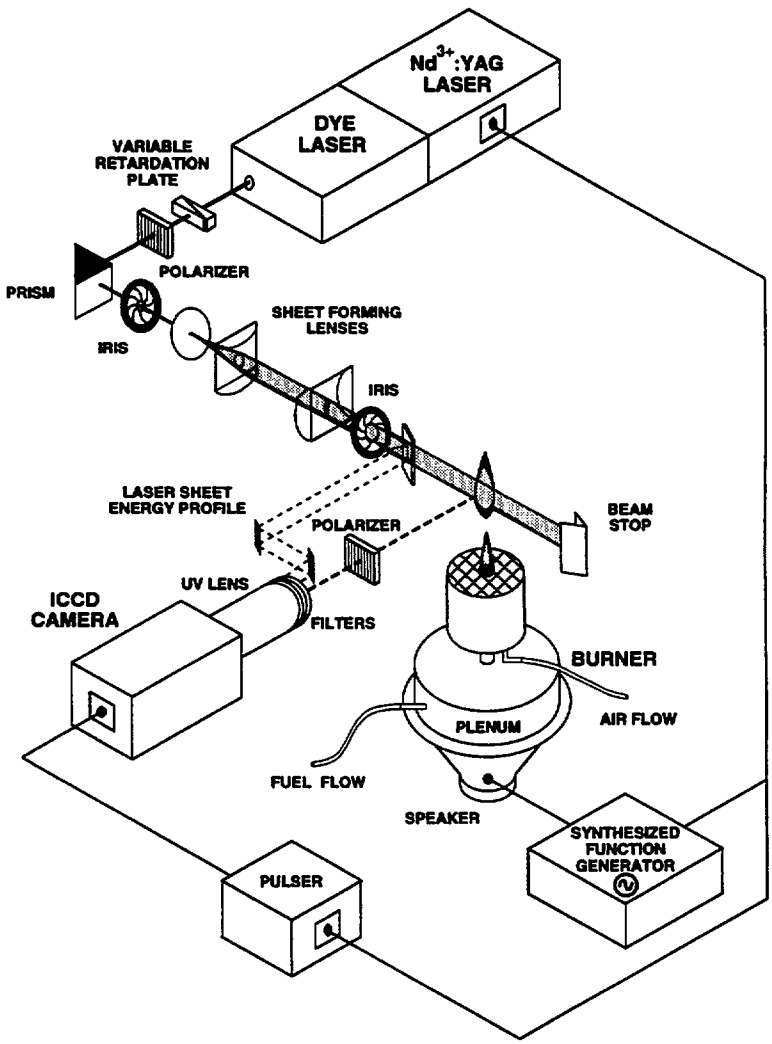

Fig. 1. Experimental set-up for 1-D or 2-D imaging of axisymmetric diffusion flames which are acoustically excited and phase locked to the pulsed dye laser system operating at 10 Hz. For the laser-induced incandescence experiments, the polarizing elements and sheet-forming optics are removed, and a 300-mm focal length lens is used to focus the beam at the center of the flame. The coannular burner is mounted on a vertical translation stage, allowing 2-D measurements to be performed from the burner lip up to a height of 13.4 cm.

TABLE 1

Conditions for Coflowing, Axisymmetric Diffusion Flames

Fuel	Fuel Velocity (cm/s)	Air Velocity (cm/s)	Visible Flame Height (mm)
Methane	7.8	7.9	79
Propane	2.6	8.7	85
Ethylene	4.1	8.7	91

that was vertically collimated and focused over the burner, with a beam waist of $\approx 300\ \mu m$ (full width at half maximum, FWHM) measured by imaging a highly attenuated reflection of the sheet onto the camera. Scattered light was detected as a planar image on the ICCD camera after passage through a vertical polarizer and glass filters that gave an effective bandpass of 550 to 700 nm. The image intensifier gate was set for 45 ns (FWHM, with ≈ 8

ns rise and fall times), fully opening coincident with the arrival of the laser light. With these filters and temporal gating, signals from both broadband laser-induced fluorescence (attributed to polycyclic aromatic hydrocarbons) and natural flame luminosity were much smaller than the vertically polarized soot scattering for all of the flames investigated. (For this laser wavelength, the peak of the broadband fluorescence is slightly blue-shifted relative to the excitation wavelength [37].) At sufficiently high laser energies, laser-induced incandescence was found to interfere with the scattering signals, so energies were maintained low enough (< 5 mJ/pulse output from the dye laser) to prevent excitation of the LII. An attenuated reflection of the incident laser sheet was directed to the side of the CCD pixel array, allowing shot-to-shot correction of the measured signals for the overall laser pulse energy as well as the energy variation in the vertical plane. A set of two lenses was required along the path of the reflected sheet (not shown in Fig. 1) in order to properly scale the height of the reflected sheet and bring it into focus on the CCD array.

Overlapping images were collected at five separate heights, giving measured signals from the base of the flames to a height of 134 mm above the burner lip. The CCD array used 3×3 binning for an effective spatial resolution of 250 μm in the object plane. The steady flame images were highly reproducible, so 10-shot averages were used at all heights. For the flickering flames, the bottommost images generally showed relatively small scattering signals and good reproducibility, so they were collected as 10-shot averages. Images higher in the flickering flames were collected as five single-shot "frames," due to the steep gradients within the scattering profiles and the cycle-to-cycle wobble at heights above the location of flame clip-off. The use of different burner exhaust flows and surrounding screens (to dampen laboratory air currents) did not appreciably affect the measured intensity of the side-to-side flame wobble—i.e., the wobble appears to result from inherent flame instabilities and sensitivity to any asymmetry associated with the flame clip-off event.

After normalization for the measured local beam energy intensity, individual radial profiles of scattering were analyzed at 5-mm increments in the axial direction. Two-row averages (i.e., 0.5 mm in the vertical dimension) of scattering were considered, in order to improve the agreement with the LII measurement heights for use in the Mie analysis. In general, it was found that the profiles from different single-shot frames at a given phase and height showed excellent agreement, once minor left-to-right shifting (typically 1 to 4 binned pixels) had been performed on the profiles in areas of the flame with significant wobbling. In some images, particularly high in the flickering flames, the flame moved far enough away from the plane of the laser sheet that the resulting profiles were narrower than for other images; in such instances, only the widest, most consistent profiles were used to construct the final average.

The scattering signals were calibrated by using an unexpanded, focused laser beam to image the soot scattering at low heights in the steady methane/air flame and then comparing the soot scattering intensity to the Rayleigh scattering from ambient-temperature propane and methane issuing from the fuel tube, surrounded by coflowing air. Rayleigh cross sections were calculated using

$$\sigma(90°) = \frac{4\pi^2(n-1)^2}{N^2\lambda^4}\frac{3}{3-4\rho}, \qquad (1)$$

where n is the index of refraction, N is the gas number density, λ is the wavelength of scattered light, and ρ is the depolarization ratio (which equals zero for isotropic molecules). Indices of refraction were calculated at 560.3 nm (and 25°C) from the Landolt–Börnstein tables [38], and depolarization ratios were taken from measurements at 632.8 nm by Bogaard et al. [39] for N_2 and C_3H_8, and by Bridge and Buckingham [40] for O_2. With these values, the propane scattering cross section is 6.48×10^{-27} cm^2/sr, and the expected ratios of scattering for propane, methane, and air are 13.3 : 2.2 : 1. The measured ratios of scattering using line averages on the CCD camera were found to be $12.2(\pm 1.3) : 2.2(\pm 0.3) : 1$.

The measured soot scattering signals were corrected for extinction of the incident laser beam through the flame due to high soot con-

centrations. Similarly, a correction was applied for extinction of the scattering signal itself between its point of origin, in the plane of the laser sheet, and the detector, which is located perpendicular to that plane. Since the scattering signals are normalized by the energy distribution of the incident laser sheet, correction for laser beam extinction simply involves division of the energy-corrected signals by

$$\int_{e^{-\infty}}^{R} - K_{ext}(r)\, dr, \tag{2}$$

where the extinction coefficient for soot is given by

$$K_{ext} \approx K_{abs} = f_v \frac{6\pi E(\tilde{m})}{\lambda}, \tag{3}$$

where f_v is the soot volume fraction, λ is the laser wavelength, and

$$E(\tilde{m}) \equiv -Im\left(\frac{\tilde{m}^2 - 1}{\tilde{m}^2 + 2}\right) \tag{4}$$

is a function of the soot index of refraction, $\tilde{m}$. The index of refraction is assumed to be $1.57-0.56i$ for consistency with a large number of soot studies[1]. This expression for K_{ext} is strictly valid only for soot particles in the Rayleigh limit, wherein particle scattering is negligible with respect to absorption. For conditions in which the scattering contributes significantly to the extinction caused by soot, Eq. 3 will in theory underpredict the extinction correction. The radial profiles of the soot volume fractions necessary for this correction are given by the final, fully corrected LII signals. The integral in Eq. 2 was calculated using trapezoidal areas for the 0.25-mm-spaced LII profile points.

For an axisymmetric soot field, the differential extinction coefficient between the optical signal excitation (along a line) and the detection plane can be shown by geometric arguments to be

$$K_{ext}(r) = \frac{f_v}{\sqrt{1 - \left(\frac{R}{r}\right)^2}} \frac{6\pi E(\tilde{m})}{\lambda} \tag{5}$$

for a signal originating from a position $r = R$ from the flame centerline. The relevant geometry for derivation of this expression is shown in Fig. 2. The expression for the scattering signal extinction correction is then given as

$$Q_{vvc} = \frac{Q_{vv}}{\exp\left(\int_{-\infty}^{R} - \frac{f_v}{\sqrt{1 - \left(\frac{R}{r}\right)^2}} \frac{6\pi E(\tilde{m})}{\lambda} dr\right)} \tag{6}$$

for positions to the left of the centerline, and

$$Q_{vvc} = \frac{Q_{vv}}{\exp\left(\int_{R}^{+\infty} - \frac{f_v}{\sqrt{1 - \left(\frac{R}{r}\right)^2}} \frac{6\pi E(\tilde{m})}{\lambda} dr\right)} \tag{7}$$

for positions to the right of the centerline, where Q_{vv} is the scattering signal previously corrected for laser beam extinction and Q_{vvc} is the scattering signal corrected for both signal extinction and laser beam extinction. The values of the computed integrals in Eqs. 6 and 7 depend strongly on the proximity of the nearest grid point to the radial position of the scattering signal, R, due to the singularity of the integrand at $r = R$. Consequently, the integral was evaluated by using trapezoidal areas for the 0.25-mm-spaced LII soot volume fraction up to the radial node adjacent to R, and then the interpolated area between R and $R + 1$ was determined by using $20\times$ finer spacing. This approach resulted in agreement between the computed extinction and the measured line-of-sight extinction to within 4%, when the soot volume fractions in the extinc-

[1] $\tilde{m} = 1.57-0.56i$ has been widely misattributed to Dalzell and Sarofim [41], who reported mean values of $1.56-0.46i$ for acetylene soot and $1.57-0.50i$ for propane soot at visible wavelengths (see Ref. 42). Use of any of these values for the index of refraction yields an extinction coefficient which is in good agreement with most of the literature values for visible wavelengths.

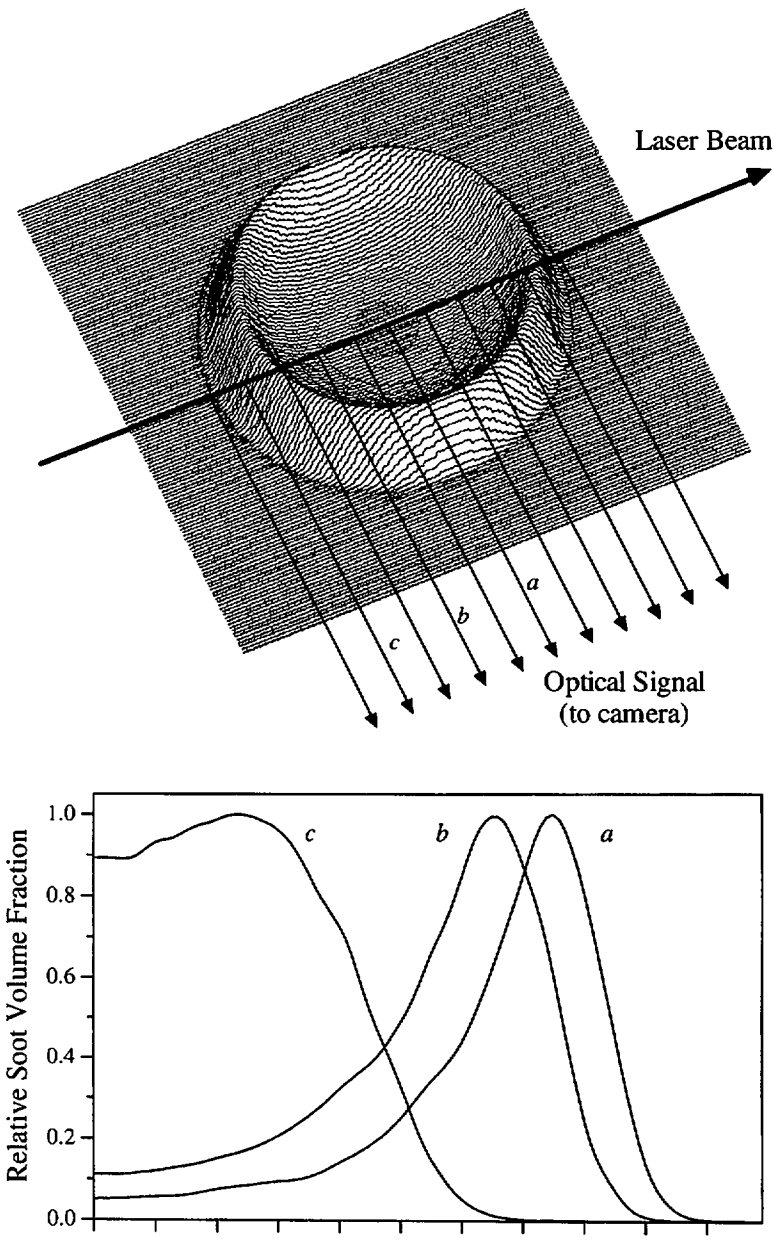

Fig. 2. Top: Three-dimensional "surface plot" view of the soot concentration in the horizontal plane formed by the laser beam and the ICCD camera. The soot profile used here is a cubic spline fit to data collected at mid-height in a methane/air flame. Bottom: Laser-excited signals originating from the flame centerline (ray *a*) traverse the actual soot radial profile en route to the detector, whereas signals originating from locations away from the centerline (rays *b* and *c*) traverse distorted soot profiles.

tion calculation were derived by tomographically inverting the measured extinction with the three-point Abel technique [43].

The laser beam extinction and scattering signal extinctions are negligible for the steady methane flame due to its low soot concentrations, but become significant for the flickering methane flames and, especially, for all of the propane and ethylene flames. A typical correction is shown in Fig. 3 at mid-height of the

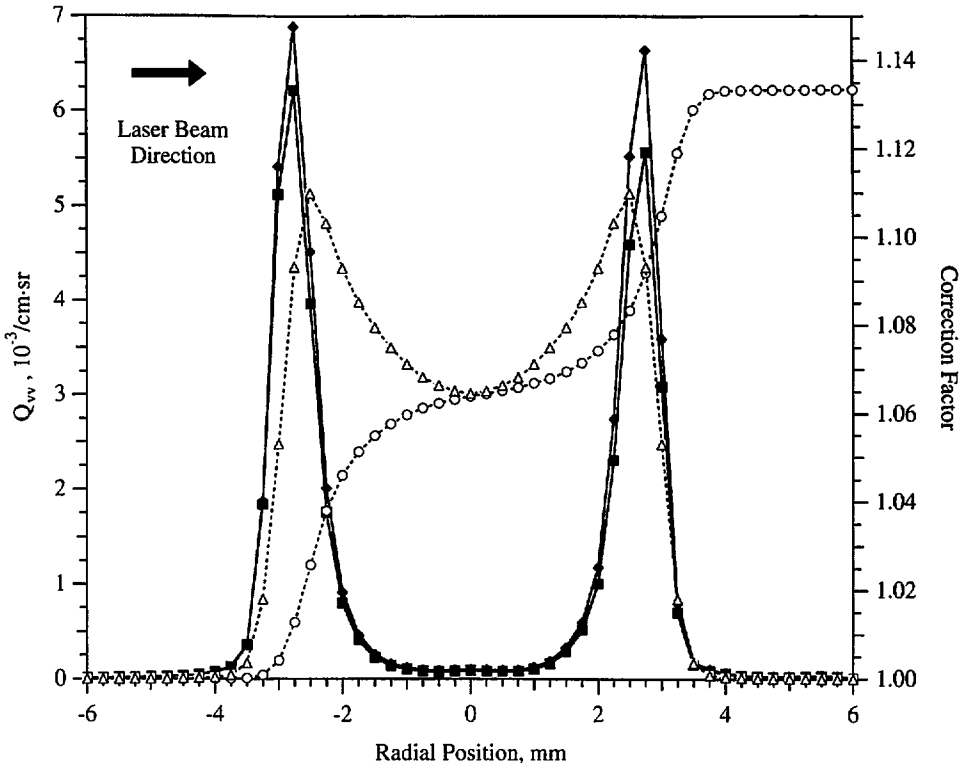

Fig. 3. Effect of computed laser beam and signal extinction corrections on the calibrated 560.3-nm scattering profile measured at H = 40 mm above the burner lip in the steady propane flame. The uncorrected (■) and corrected (◆) scattering signals are shown as solid lines, and the individual contributions of the laser beam extinction correction (○) and scattering signal extinction correction (△) are shown as dashed lines.

steady propane flame. These types of extinction corrections are, in principle, necessary for any optical measurement in flames with heavy soot loadings ($\geq$ 1 ppm, i.e., 10^{-6} cm^3/cm^3) or long soot path lengths. For point measurements with fixed detection optics, however, the functional form of the laser beam and signal extinction corrections can be reversed from those presented here, for example, when profiles are taken by translating the burner perpendicular to the direction of laser beam propagation.

2.3. Laser-Induced Incandescence

Laser-induced incandescence of soot particles was excited by focusing the 560.3-nm dye laser beam with a spherical 300-mm focal length lens. The incandescence signal was recorded as a line image on the ICCD camera. No pixel binning was used on the camera, resulting in a pixel spacing of 83 μm. As with the scattering signals, at low heights in the flames the LII signals were generally small and showed good reproducibility, so they were collected as 10-shot to 100-shot averages, depending on the particular height and fuel. Starting at H = 25 mm above the burner lip for propane and ethylene and at H = 45 mm for methane, the LII signals were measured as 10 single-shot frames, in order to allow subsequent minor left-right alignment of single-shot profiles to correct for the effects of flame instability.

2.3.1. Spectral Detection

LII involves the rapid heating of soot particles to temperatures at which their resultant incandescence can be distinguished, through the use of temporal gating and wavelength filtering, from the natural luminosity arising from the flame and from broadband laser-induced fluorescence (LIF). For practical implementation, the soot particles are typically heated to their vaporization point (3915 K is the vaporization

temperature for graphite [44]) or even to higher temperatures (up to ≈ 5000 K) during each laser pulse [45–47]. At these temperatures, the LII spectrum exhibits a maximum at visible wavelengths and extends from the near IR region to the near UV. Background luminosity signals are characteristic of soot temperatures in the range of 1600 to 2000 K and, as such, peak in the infrared, with much lower instantaneous intensity than the LII signals.

Unfortunately, significant C_2 emission can arise when using laser fluences characteristic of LII excitation at wavelengths between the $\Delta v = 0$ Swan band of C_2, with a bandhead at 516.5 nm, and the $\Delta v = -1$ Swan band, with a bandhead at 563.6 nm [48, 49]. The Swan bands extend from ≈ 420 to 620 nm, as shown in Fig. 4, where the C_2 spectrum has been simulated using vibrational and rotational constants from Huber and Herzberg [50] and Franck–Condon factors from Tyte et al. [51]. While there is some evidence that resonantly excited C_2 LIF signals from vaporized soot are proportional to the soot volume fraction for high laser fluences [48, 49], our experiments revealed that these signals saturate for soot concentrations greater than 2 ppm for the laser intensity used in our LII imaging. Furthermore, the dependence of nonresonantly excited C_2 LIF on soot volume fraction is unknown, and C_2 LIF signals can arise from the photodecomposition of large molecules as well as soot particles [6, 48, 49, 52]. Hence, in the present study, the C_2 fluorescence represents contamination of the soot volume fraction information carried by the LII. A monochromator spectral scan was conducted in a steady ethylene/air flame using the same laser wavelength and intensity as for the LII measurements, and revealed the presence of significant C_2 emission in the $\Delta v = 0$ and Δv

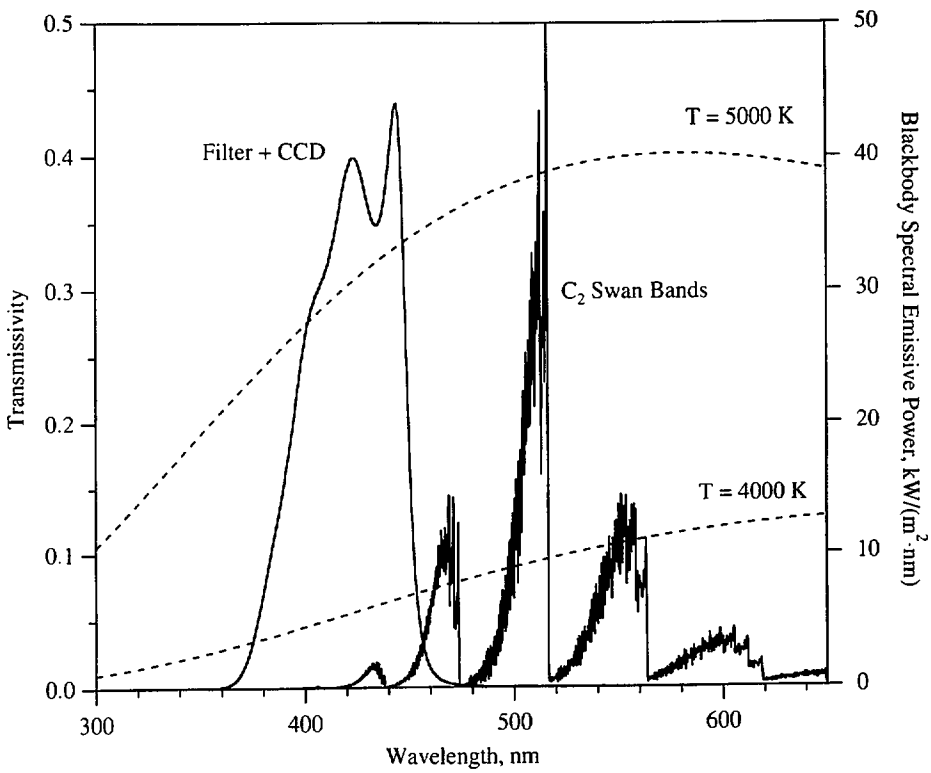

Fig. 4. Spectral characteristics of the LII imaging filter (multiplied by the CCD cathode sensitivity curve) used in the present study, as well as C_2 LIF Swan-band interferences and blackbody radiation curves for 4000 and 5000 K, which are temperatures characteristic of the peak LII signals. The C_2 emission spectra have been computed assuming vibrational and rotational temperatures of 4000 K and an effective detector resolution of 6.6 cm^{-1} throughout the wavelength range. The peak C_2 emission at the 516.5-nm bandhead is scaled to a value of 0.5 on the transmissivity scale.

$= \pm 1$ Swan bands (516.5, 473.7, and 563.6 nm, respectively). No appreciable C_2 emission signals were detected at shorter wavelengths.

A short-pass dielectric 450-nm filter was used for detection of the LII, which, when combined with the cathode sensitivity curve of the CCD, yields the detection curve shown in Fig. 4. Detection of the LII at wavelengths significantly blue-shifted from the excitation wavelength eliminates any possible contribution from laser light scattering and also minimizes possible contributions from broadband LIF, which peaks in the vicinity of 550 nm for the excitation wavelength used here [37]. Furthermore, detection at short wavelengths minimizes interferences from natural flame luminosity, which can be a predominant concern in some highly sooting environments such as diesel engines [53]. As is evident from Fig. 4, the LII signal intensity decreases rapidly below 400 nm, so the chosen short-pass filter represents an appropriate compromise between LII signal strength and discrimination against sources of interference. The nominal bandpass of the glass filter used in our previous imaging of LII [14] was 320 to 440 nm, but included some transmission to longer wavelengths (the transmittance is 0.17 at 460 nm and 0.01 at 480 nm). Thus, this previous filter possibly transmitted significant nonresonant C_2 LIF contributions through the $\Delta v = +1$ Swan band. In addition, light was passed at wavelengths greater than 720 nm, necessitating luminosity corrections to the measured LII profiles which are not required in the current study with the short-pass dielectric filter.

The detection wavelength plays a role in the size dependence of the LII measurement. Melton [46] solved a simplified energy balance at the peak of the laser pulse for soot particles in the Rayleigh limit with respect to both laser absorption and thermal emission detection. With these assumptions, the incandescence signal is proportional to $d^{(3+[\approx 0.154/\lambda_{det}(\mu m)])}$ ($\approx d^{3.37}$ for our detection filter), where the second term in the exponent results from the size dependence of the maximum particle temperature for Rayleigh absorbers. Based on this result, detection at long wavelengths (ignoring other considerations for the moment) would seem to be desirable in order to most closely realize the desired proportionality to particle volume. However, for detection wavelengths and particle sizes which exceed true Rayleigh limit behavior, particles emit radiation on less than a volumetric basis (i.e., the relevant emission cross section is given by $C_{em} \propto d^{2+}$ instead of $C_{em_{Rayleigh}} \propto d^3$), so in this case the incandescence signal more accurately follows d^3 than the Melton expression might suggest. In addition, the actual superheat temperatures attained by soot during the laser pulse and the effect of particle size on these peak temperatures are not well known, so the expression by Melton should only be considered a rough estimate.

2.3.2. Fluence Dependence

An important aspect of laser-induced incandescence which lends itself to use in imaging soot distributions in turbulent environments (in addition to its high temporal resolution and close proportionality to soot volume fraction) is its weak dependence on laser energy, once a threshold level has been reached. For nanosecond laser pulses, soot particle sizes larger than ≈ 10 nm but smaller than ≈ 200 nm, and temporal detection gates longer than the laser pulse duration, the key quantity which determines the power dependence is laser energy fluence—i.e., the integrated laser intensity, or energy flux, over the duration of the pulse [54, 55]. For these conditions, the energy fluence is more important than the peak laser intensity since energy conduction within the soot particles is over an order of magnitude faster than the laser pulse duration [55, 56] and, once the soot particle is heated to near its vaporization point, heat loss during the laser pulse is dominated by evaporation rather than by conductive or radiative heat loss [46, 55, 57, 58]. Therefore, energy loss from the soot is sensitive to the total energy absorbed rather than to the peak particle temperature. A number of recent papers on LII have reported power dependences as a function of laser intensity (W/cm^2) and termed this "laser fluence," when in fact the actual laser energy fluence (J/cm^2) is both more accurately estimated and the quantity of most interest.

As a single soot particle is excited by an increasing energy fluence, its temperature will

rapidly rise during the laser pulse until the absorbed energy is such that the particle reaches its vaporization point. Increasing the energy fluence past this level may result in some superheating of the particle during the duration of the laser pulse, but at the end of the laser pulse, the particle temperature will rapidly drop back to its vaporization point, vaporization will quickly decrease, and the temperature will begin an exponential decay toward that of the surrounding gas. Consequently, as the laser fluence is increased, the incandescence from a single particle should show a rapid rise until the particle begins to vaporize, a leveling off as the peak particle temperature remains approximately constant with increasing laser energy fluence, and then eventually a decrease as the mass loss due to vaporization reduces the amount of radiation emitted over the duration of the detection sampling time.

Experimentally, the single-particle behavior described above can, in principle, be investigated by applying a spatially uniform (i.e., a "top hat" or rectangular profile), fixed-size beam to a volume of relatively monodisperse particles. In fact, Ni et al. [59] have measured a fluence dependence for a rectangular-profile beam which shows a rapid rise, rounded peak, and gradual tail-off at higher energy fluences, in good agreement with the power dependence calculated by Tait and Greenhalgh for such a beam [57]. In general, however, LII excitation is induced with beams which are at least approximately spatially Gaussian. As the beam intensity is increased for a Gaussian beam, the effective sampling volume over which the local energy fluence is greater than the LII threshold grows, counteracting the effect of mass loss in the center of the beam and tending to flatten the overall post-threshold fluence dependence. Indeed, Santoro and co-workers [47, 59], Tait and Greenhalgh [57], and Bengtsson and Aldén [49] have all measured either flat or slightly upsloping "plateau" regions for Gaussian beams, in general agreement with the calculation by Tait and Greenhalgh. Vander Wal and Weiland [60] and Case et al. [61], in contrast, have measured rounded LII power dependences for reported Gaussian beams. However, in the first case the detection optics were deliberately set up to minimize wing contributions to the LII signal [62], and in the second study, the power dependence may have been influenced by the wide range of particle sizes and high content of condensed species on the diesel exhaust soot being excited.

For our measurements of the LII fluence dependence, the incident laser energy was varied by using a Babinet–Soleil compensator to incrementally rotate the polarization of the laser beam before passage through a fixed polarizer. For the lowest energies, a glass filter with a measured transmittance was also used to attenuate the incident beam. A pyroelectric joulemeter, with a neutral density filter providing attenuation at high energies, monitored the shot-to-shot laser pulse energy and was calibrated to a volumetric absorber. LII signal intensities were measured by binning across the horizontal width of the soot region imaged with the ICCD camera using the 450-nm short-pass filter, after background dark counts had been subtracted. Cross sections of a multiple-shot Rayleigh scattering image in air gave Gaussian profiles across the entire 48-mm image width. Figure 5 shows the LII fluence dependence measured in the steady CH_4/air and C_2H_4/air flames, using both a short (19 ns) and mid-length (85 ns) detection gate on the ICCD camera. As is evident, the fluence dependence of the LII signals is similar in the CH_4 and C_2H_4 flames despite significant differences in soot particle size (60 vs. 100 nm, based on our Mie analysis in Section 4 below), number density (2.4 vs. $8.3 \times 10^9/cm^3$), and, most likely, morphology at these measurement locations. Likewise, significant differences in the length of the detection gate influence only slightly the fluence dependence. In fact, a fluence dependence measured over the lower one-third of the range shown in Fig. 5 for a 1100-ns detection gate in the C_2H_4 flame, which includes essentially all measurable LII signal, agrees with the C_2H_4 data for an 85-ns detection gate.

The measured fluence dependence exhibits the expected flattening behavior after rising sharply to a threshold fluence. The post-threshold fluence dependence shows a stronger positive slope than generally reported elsewhere [47, 49, 59, 60]. Differences in the rela-

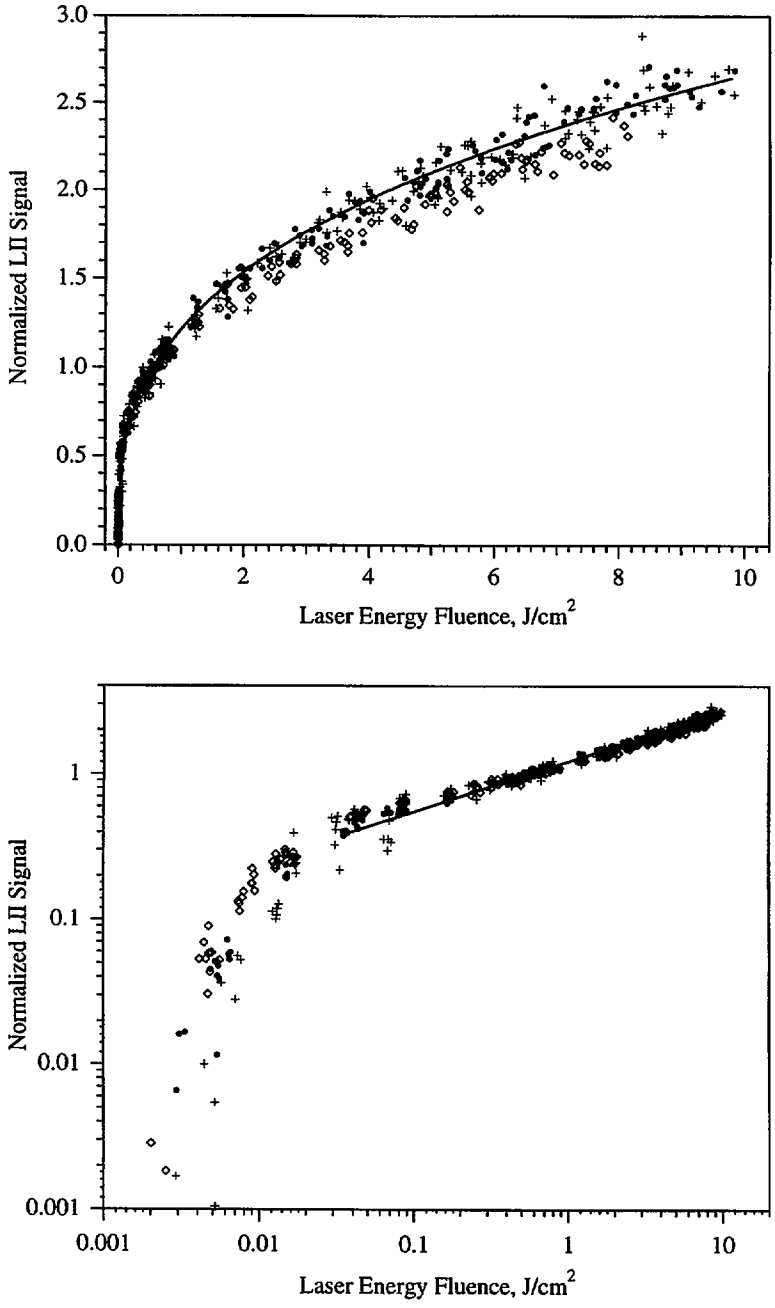

Fig. 5. Fluence dependence of LII measured in steady laminar diffusion flames presented on linear (top) and logarithmic (bottom) bases. Data were collected at H = 20 mm in the ethylene/air flame for detection gate durations of 19 ns (+) and 85 ns (◇)—both gates opening coincident with the arrival of the ≈ 5-ns laser pulse. Data are also shown for the methane/air flame at H = 50 mm with the 85-ns gate (•). Raw signals for each condition have been normalized to a value of 1.0 at a fluence of 0.6 J/cm^2. The solid line shown is the least-squares power-law fit of the methane data for fluences greater than 0.03 J/cm^2; the fit follows the expression signal ∝ fluence$^{0.34}$.

tive widths of the laser beam and the detector depth-of-field (discussed below) or in the laser beam shape may account for the flatter behavior of the power dependence reported by some other investigators. In order to minimize any possible contributions of increased beam size in the vertical direction to the measured post-threshold slope, both the fluence dependences shown here and the actual LII profile data were analyzed by summing only the peak two horizontal pixel rows of the CCD images, corresponding to a vertical binning of 167 μm.

The threshold fluence evident in Fig. 5 appears markedly different depending on the scale of the plot. For linear scales, the threshold fluence is difficult to define, but would appear to lie between 0.2 and 0.8 J/cm^2. On the other hand, the logarithmic plot shows that the power-law fit to the data is valid for fluences greater than 0.1 J/cm^2, and the fluence threshold occurs at $\approx$ 0.03 J/cm^2. The logarithmic plot more accurately defines the critical fluence for the onset of soot particle vaporization, while the linear plot conveys the minimum fluence required in order to obtain a small change in the LII signal for a given *absolute* change in laser fluence. Dasch determined 0.2 J/cm^2 to be the threshold fluence for measurable evaporation from in-flame soot [55], and conversion of reported LII threshold intensities reported by other workers to fluences yields consistent values of $\approx$ 0.1 to 0.2 J/cm^2 [49, 57, 59, 61]. Use of our measured FWHM of the Rayleigh scattering profile (225 μm) to calculate fluence gives values 2.0 times larger than those presented in Fig. 5, but even with this consideration, our threshold fluence appears somewhat lower than that found by others. In fact, the beam diameter over which significant LII signal arises changes with beam intensity and is likely to be larger than the measured FWHM for most of the fluence range shown in Fig. 5. The beam diameter assumed here for the calculation of fluence is 317 μm, which is that estimated over which incandescence is excited at the fluence level used for obtaining the LII data (see Section 2.3.4 below).

The incident laser fluence used for LII measurements in the present study was sufficiently high (5.0 J/cm^2) that even with substantial extinction of the beam through the flame, the fluence was always well above the threshold value. Laser pulse energy information was stored with each LII file, so the fit to the fluence dependence curves shown in Fig. 5 could be used to correct for shot-to-shot variations in laser energy and in-flame beam extinction effects on the LII signals. The standard deviation in the laser pulse energy for these experiments was measured to be $\pm$5%, and the total measured variation was within $\pm$10% of the mean. Based on the measured fluence dependence, this corresponds to a maximum correction of $\pm$3.5% to be applied to the LII signals, which was deemed insignificant. For the propane and ethylene flames, the beam extinction can be substantial, up to $\approx$ 30%, leading to a potential correction of $\approx$ 10% for the LII signals originating from the edge of the flame that the laser beam exits. However, appreciable left-to-right asymmetries in the LII profiles were generally not evident, even for flame locations with large soot volume fractions ($>$ 5 ppm), so this correction was not applied. Significant vaporization of particles in the center of the beam may have occurred during the laser pulse and would have reduced the overall extent of beam extinction through the flame [49].

2.3.3. Detector Gate Width and Timing

An 85-ns detection gate, opening coincident with the arrival of the laser pulse, was employed on the ICCD camera in collecting the LII profiles. This relatively long gate was chosen in order to improve the signal-to-noise ratio for imaging low soot levels in the methane flames with the use of the relatively narrowband short-pass 450-nm filter. An additional benefit of employing a collection gate which is significantly longer than the laser pulse duration is enhanced discrimination against broadband fluorescence and laser-excited C_2 LIF, whose signals rapidly decay shortly after passage of the laser pulse [49, 63]. However, both computations [46, 57] and limited experimental evidence [59] suggest that the use of long detection gates biases the LII measurement toward larger particles, since they cool more

slowly (due to their reduced ratio of surface area to volume) after the initial laser pulse excitation.

In order to assess the potential effect of gate duration on the LII profiles, measurements were performed in the steady ethylene/air flame for detection gates of 19, 85, and 1100 ns, all opening coincident with the laser shot. Upon normalizing the profiles for peak intensity at midheight in the flame, the shortest gate gives signals $\approx 30\%$ higher than the other gates at low heights ($H \leq 20$ mm above the burner surface). Near the top of the flame ($H \geq 70$ mm), signals using the shortest gate are 10 to 25% higher than those for the mid-length gate, and over 50% higher than those for the longest gate. Calculated Mie diameters in this flame (discussed in Section 4.3) vary from ≈ 60 nm at $H = 10$ mm to 100 nm at $H = 20$ mm, with only small variations ($90 \leq D \leq 115$ nm) until $H = 80$ mm (where $D \approx 70$ nm). On the basis of these small changes in the optical particle diameters, the differences in the LII signals with gate length seem unexpected at $H = 20$ mm and $H = 70$ mm. However, the relevant length scale for the physical processes of concern to LII (predominantly laser absorption, carbon vaporization, and thermal emission) is likely to be that of the primary soot particles, not the optically determined Mie diameter representation of the agglomerated primary particles. Thermophoretic sampling of the soot in the Non-Smoking ethylene/air flame (nearly identical to that considered here) has revealed a significant increase in the primary particle size from $H = 20$ mm to $H = 30$ mm (22 nm vs. 32 nm) and a significant decrease from $H = 60$ mm to $H = 70$ mm in the annular region (27 nm vs. 19 nm [64]). Along the centerline, the primary particle size also decreases from 28 nm at $H = 50$ mm to 21 nm at $H = 70$ mm [65]. These results support the concept of gate-length effects being tied to the primary particle size.

The measured extent of variation in the relative LII signals found for the 19-ns and 85-ns detection gates in the ethylene flame suggests that an appreciable size bias exists when using the 85-ns gate. However, an LII signal calibration based on laser extinction measurements in the steady methane flame (at a height where $d_{Mie} = 50$ nm and $d_{primary} < 20$ nm [11]) is found to work well for LII measurements in the steady ethylene flame, as demonstrated in Section 2.3.5. Therefore, while the evidence is somewhat inconclusive, the 85-ns detection gate probably biases the LII measurement somewhat to larger particles (presumably on the scale of the primary particles) and therefore biases against soot volume fractions at low heights and in the soot oxidation regions.

Cignoli et al. [63] have advised time-delayed detection of LII, in order to eliminate contributions from broadband fluorescence. However, for our choice of excitation and detection wavelengths, this was not necessary. The LII images show strong signals only in flame regions where soot scattering is measured, even when significant broadband fluorescence is imaged in regions interior to the soot layer. Furthermore, efforts to measure any fluorescence signal through the LII spectral filter at fluences just below that required for LII proved unsuccessful, and broadband fluorescence saturates at moderate laser intensities at moderate powers. As mentioned above, use of a delayed detection gate is undesirable because it biases the LII measurements in favor of large soot particles [46, 57, 59]. Our analysis disagrees diametrically with the recommendations of Vander Wal and Weiland [60] for signal collection over as wide a spectral and temporal bandpass as possible.

2.3.4. Radial Dependence of Signal Strengths

Due to the weak fluence dependence of LII signals above the threshold fluence, increasing the width of the laser beam (e.g., by collecting data away from the beam focal point) results in an increase in the LII signal for detection systems in which either the sampling depth-of-field or the vertical component of the detection volume is greater than the laser beam width at the measurement location. This behavior is in marked contrast to that experienced for linear excitation processes, wherein the beam width does not affect the signal intensity for a constant pulse energy, or for multiphoton processes whose excitation rates rise faster than

linearly with the laser intensity, for which defocusing the beam always results in a lower signal. Focused beams are generally desirable in LII measurements in order to achieve an energy fluence significantly greater than the LII threshold level and for purposes of attaining good spatial resolution. For imaging applications such as those considered here, this aspect of LII generally results in a variation in the effective sensitivity for the detection of LII along the laser beam (i.e., radially across the flame).

In the present experiments, the camera lens depth-of-field was nominally ± 2 mm, which is significantly larger than the focused beam size throughout the plane of measurement. Furthermore, two vertical pixels were summed together, giving a nominal vertical resolution of 170 μm ($\approx$ half the value of the effective beam waist, see below). As a consequence of this spatial averaging, the LII signal originating from a given flame location (i.e., from a given soot volume fraction) was found to vary significantly as a function of distance from the beam focus. The radial variation of the LII signal was measured by translating the burner along the laser beam, with fixed excitation and detection optics, resulting in the functional dependence shown in Fig. 6. For soot concentrations measured 10 mm from the burner centerline (e.g., in the strongly flickering CH_4/air flame), the relative error in the signal is significant, $\approx$ 20%, as estimated from the quadratic fit to the data. This measured radial dependence was used to correct the raw LII signals before further analysis. The correction was particularly important for the analysis of the flickering flame signals at high heights above the burner, where the flame can be quite wide, and cycle-to-cycle wobbling of the clipped-off flame resulted in soot being detected up to 15 mm from the burner centerline. Figure 7 illustrates this radial dependence correction by presenting raw and corrected LII signals for measurements in a flickering methane/air flame. For comparison, the corrections which result from

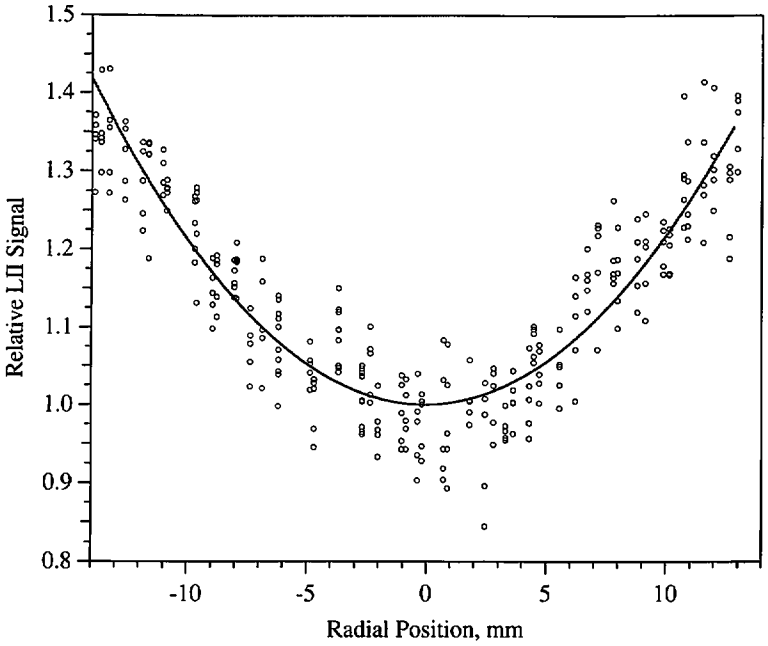

Fig. 6. Radial dependence of laser-induced incandescence signals for the experimental conditions employed to measure the LII profile data. The circles denote signal intensities measured at $H = 20$ mm in the steady ethylene flame as the burner was translated along the laser beam, and the line is a quadratic fit to the data. A quadratic fit is quite accurate within 15 mm of the focal point, whereas the LII signals farther away showed less than a quadratic dependence with radius. The relative LII signals were determined by summing the peak two horizontal pixel rows of the images (as was done to analyze the LII profile data) and then summing the peak 0.5 mm of signal across the soot layer, which is narrow at this height. For collection of LII profile data, the laser focus was set to be precisely at the burner centerline.

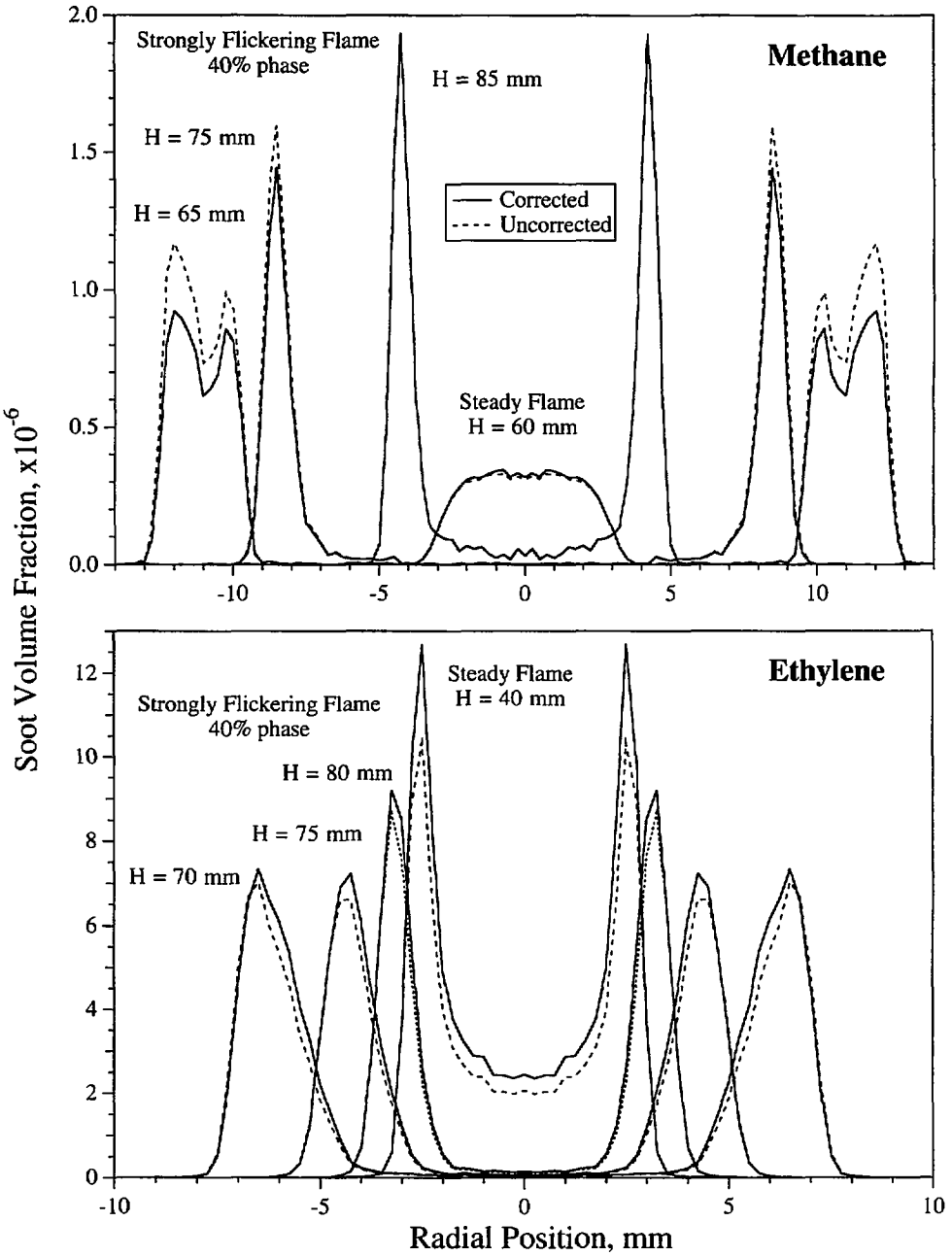

Fig. 7. Corrected and uncorrected laser-induced incandescence profiles illustrating the different effects due to beam focus/spatial averaging (the radial correction) and signal extinction considerations. Top: In the strongly flickering methane flame, the LII profiles can extend over a wide radial domain, necessitating a significant correction for the local area of the laser beam. Low soot levels render the signal extinction correction negligible. Bottom: The radial extent of the strongly flickering ethylene flame is reduced relative to methane, but the soot concentrations are ≈ 6 times larger at this location, requiring correction for signal attenuation due to soot extinction. All LII profiles have been symmetrized (i.e., averaged about the centerline).

extinction of the LII signal due to high local soot volume fractions are also shown, in this case for an ethylene/air flame. Note that in the first example the corrected LII profile at large radial locations is lower than that originally measured, whereas signal attenuation effects act in the opposite direction (see Section 2.3.6 below).

An approximate model of the effect of beam expansion on the measured LII signal strength can be obtained by calculating the D^2 dependence of the measured Rayleigh scattering cross sections, assuming different LII threshold intensities—in essence, approximating the LII power dependence as a step function over the range of fluences present across the laser beam cross section. This computation yields a radial dependence whose functional form agrees with the measured LII radial dependence for an assumed threshold intensity of approximately one-quarter of the peak focal-point fluence. With this intensity threshold, the effective beam waist for LII excitation is 317 μm. As mentioned previously (Section 2.3.2), this value of the beam diameter was used to convert measured pulse energies to average fluence values.

The extent of the radial effect correction described here is highly experiment dependent, as it varies with the depth-of-field properties and vertical resolution of the detection lens system employed and the detailed focal characteristics of the laser beam. For example, minor changes of the dye laser interstage telescope resulted in a significant variation in the diameter of the focused laser beam at the burner, with corresponding large changes in the measured LII signal at any given location. The use of long focal length lenses mitigates the need for performing this radial correction, but at the expense of spatial resolution of the measurement, which can be essential in determining the structure of thin soot layers typically found in diffusion flames.

2.3.5. Soot Volume Fraction Calibration

The measured LII signals, once corrected for their radial dependence, were placed on a quantitative basis by calibration to tomographically inverted HeNe laser extinction measurements [14] of the soot volume fraction in the steady CH_4/air flame. Due to the low soot concentrations and relatively small soot particles in this flame, the measured extinction should accurately reflect the soot absorbance, as is assumed in the Rayleigh-limit deconvolution of the extinction data into soot volume fraction. Also, the effects of laser beam extinction and LII signal extinction (see next section) are negligible in this flame, and molecular absorption at 632.8 nm is expected to be insignificant at the calibration point since broadband fluorescence is very small. Due to the wide range of soot concentrations in the present study, the LII signals (as well as the 560-nm scattering signals) were collected for a lower gain setting of the CCD intensifier for the propane and ethylene flames than for the methane flames. In this way, the signal levels were maintained within the linear response region of the ICCD camera, which was determined to be from 300 to 30,000 counts (or a dynamic range of 100) for the gain settings used. LII and soot scattering signals collected for the propane and ethylene flames were normalized to the methane flame data by matching profiles measured with the different gain settings at a characteristic height in the steady methane/air flame.

As shown in Fig. 8 (left), with a single-point calibration the LII signals and deconvolved extinction soot volume fraction values show good agreement throughout the steady CH_4/air flame. The somewhat wider profiles exhibited by the extinction data likely arise from the signal averaging required in these measurements [14]. Furthermore, comparison of LII signals, calibrated in the CH_4/air flame, with extinction-derived soot volume fraction profiles in the Non-Smoking C_2H_4/air flame [66] demonstrates reasonable agreement, as shown in Fig. 8 (right). Since the agreement in this C_2H_4/air flame is excellent toward the centerline, where the soot volume fraction is relatively insensitive to small variations in measurement heights and the exact flame conditions, the differences in the annular soot layer are ascribed to slightly different flame conditions in the two laboratories. Similar to the CH_4/air flame comparison, the slightly

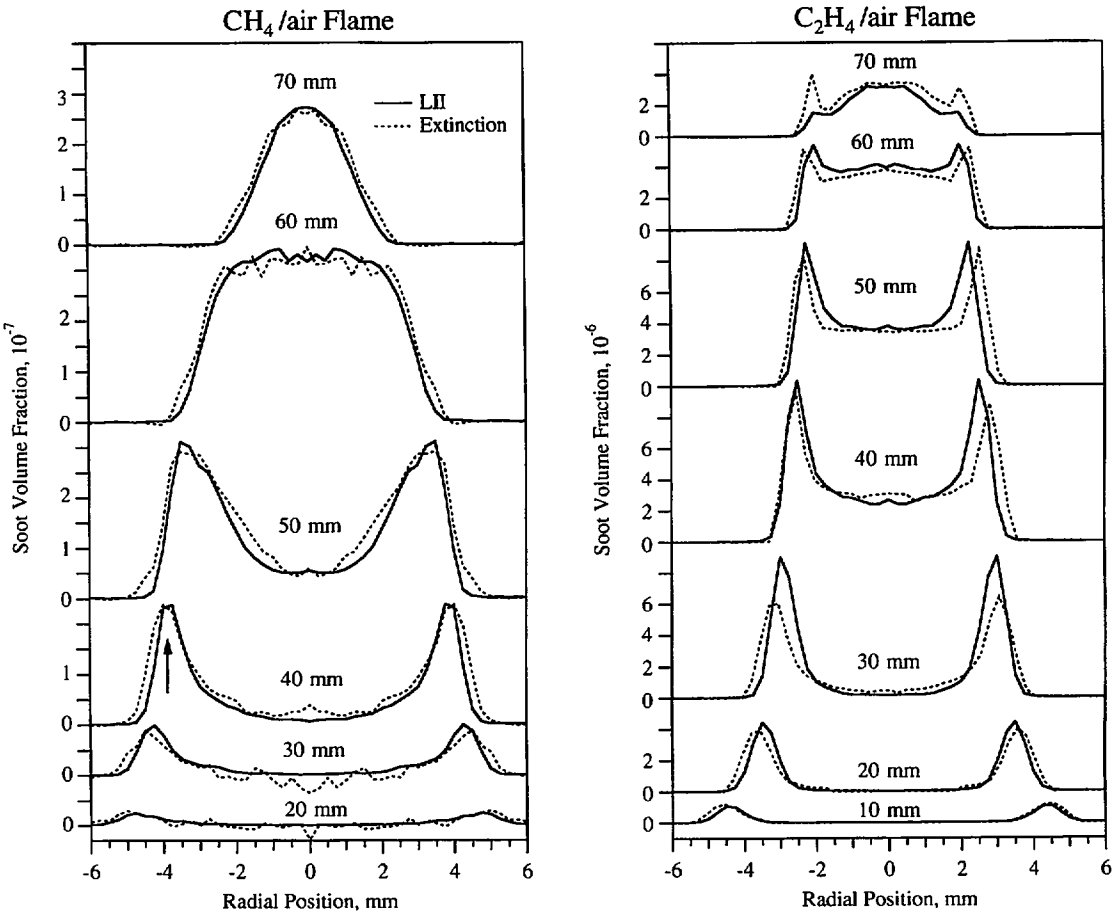

Fig. 8. Comparison of laser-induced incandescence signals and extinction-derived soot volume fractions in steady diffusion flames. Left: The LII measurements (solid lines) are calibrated to the peak soot volume fraction in the H = 40 mm profile for the CH_4/air flame (designated by the arrow). HeNe laser (632.8 nm) extinction measurements in this flame have been previously reported [14] and were tomographically deconvolved using the three-point Abel technique and an index of refraction of 1.57–0.56i. Right: LII signals from the Non-Smoking C_2H_4/air flame (fuel and air flow rates of 3.85 and 700 cm^3/s, respectively) are compared with tomographically inverted Ar-ion (514.5 nm) extinction measurements of Richardson and Santoro [66] in the same flame, using the same index of refraction. The LII and HeNe extinction measurements have been symmetrized (i.e., averaged about the centerline), and the LII signals have been calibrated to the CH_4/air flame extinction measurements as described above.

wider extinction profiles in the ethylene flames are probably due to the effects of signal averaging.

Based on these measurements, the uncertainty in the LII calibration relative to the extinction-derived soot volume fraction is approximately $\pm 10\%$ over soot volume fractions ranging from 0.05 to 10 ppm (a factor of 200), effective soot particle sizes from 30 to 115 nm (i.e., volume-equivalent spheres calculated from the Mie analysis), and number densities from 2×10^9 to 2×10^{10} cm^{-3} (assuming a monodisperse size distribution). The ability to quantitatively apply the LII measurement over such a wide range of effective soot particle sizes, extending beyond the Rayleigh limit for both the LII excitation and, especially, the detection process, may result from the agglomerated structure of the soot particles in these flames. The primary particle diameters always remain less than 40 nm [64], which is well within the Rayleigh limit.

2.3.6. Signal Extinction Correction

As discussed in Section 2.2 on our light scattering measurements, extinction of optical signals between their location of origin within the flame and the detector can be significant for

soot loadings on the order of 1 ppm. Therefore, the laser-induced incandescence signals, once corrected for radial effects, centered, binned by 3 in the radial direction (to give an effective resolution of 0.25 mm), calibrated, and symmetrized (i.e., averaged about the centerline), were self-corrected for soot extinction using Eq. 6 with $\tilde{m} = 1.57-0.56i$ and the effective LII signal wavelength taken to be 430 nm. Since this correction updated the soot volume fraction values that were used to calculate the extent of extinction, it was necessary to iterate twice for cases of strong extinction in order to reduce errors in the calculated extinction below 1%. In the steady flames, the maximum LII signal extinction correction for propane was found to be 15% at $H = 40$ mm and for ethylene was 31% at $H = 35$ mm. The maximum extinction correction in the flickering flames was 32% for ethylene. This correction is only possible in our experiments due to the axisymmetry of the flow field. For general applications in an absorbing environment, signal extinction (i.e., " signal trapping") prevents the accurate measurement of soot volume fractions using LII [53], although at least lower bound values can be obtained.

The relative uncertainties for the final LII soot concentration profiles are estimated to be $\pm 10\%$ (one standard deviation) for signal variations observed in repeat measurements, $\pm 10\%$ for the calibration to extinction profiles, and up to a 5% underestimation of the LII signal strength in regions of high soot concentrations due to neglect of the fluence dependence of LII. The possible uncertainties in the determination of absolute soot concentrations are much greater, $\pm 40\%$, due to the large range of values reported for the refractive index of soot. This uncertainty directly affects the extinction calibration and also the correction for LII signal attenuation. The variation of values for the soot refractive index is illustrated in Section 4, Fig. 13, and is discussed in Ref. 42.

3. RESULTS

Figure 9 shows images of OH· laser-induced fluorescence and horizontally polarized soot scattering in the steady methane, propane, and ethylene flames. The scattering signals reveal that the soot field is dominated by an annular structure, progressing from the weakly sooting methane flame to the most strongly sooting ethylene flame. Note that all three steady flames are clearly nonsmoking—i.e., all of the soot is oxidized in the upper flame regions. Images of the moderately flickering versions of these flames, as well as the strongly flickering methane flame, are shown in Fig. 10.The flickering methane flames clearly exhibit a strong enhancement in soot scattering relative to the steady flame. For both propane and ethylene, in contrast, the flickering flames show only a relatively small enhancement in the peak scattering intensity, *yet these flames are visibly observed to emit smoke*. The strongly flickering condition, presented only for methane, exhibits a more vigorous vortex interaction in the flame development, manifested by shorter clip-off heights and a stronger vortical roll-up which penetrates into the burning clipped-off portion of the fuel gases. The soot scattering signals apparent in images of these strongly flickering flames, however, show little difference from the levels measured in their moderately flickering counterparts.

3.1. Visible Light Scattering

Table 2 lists the peak, calibrated, extinction-corrected, vertically polarized soot scattering signals for the steady and flickering flames of all three fuels. Relative, standard uncertainties for repeat measurements of the scattering intensities are $\pm 10\%$. However, the LII and scattering values in Table 2 should only be considered representative, since they are the maxima of profiles that are spaced every 5 mm in the axial direction and only interrogate every 10% of the flickering flame phase cycle. In general, values similar to these peak magnitudes were measured over several heights and phases. Once normalized for the λ^{-4} Rayleigh-limit wavelength dependence, the peak scattering intensities determined for the steady methane and ethylene flames agree quite well with the most recent Ar-ion (514.5 nm) measurements of Santoro and co-workers [66] for the same nominal methane flame and their slightly shorter Non-Smoking ethylene

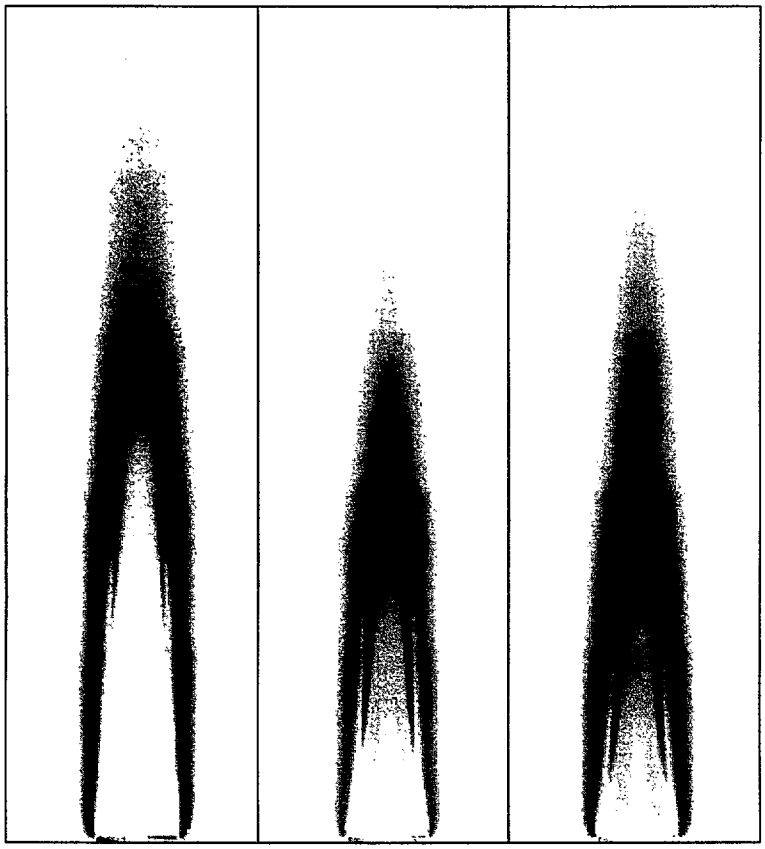

Fig. 9. Energy-corrected OH· laser-induced fluorescence and soot scattering images in the steady methane, propane, and ethylene flames using horizontally polarized light at 283.55 nm. This laser wavelength was produced by frequency doubling the output of the dye laser shown in Fig. 1. In order to view the OH· signals and scattering on the same scale, different long-pass filters were used to attenuate the widely varying soot scattering intensities in the different flames. The OH· fluorescence signals, which surround the scattering from the soot particles, have not been corrected for local quenching rates, and hence serve as a convenient, qualitative marker of the high-temperature reaction zone. For the full-height images presented here, five 10-shot average images (32 mm high) have been stacked with some overlap.

flame. As one would expect based on sooting tendencies, the ethylene flames showed the highest scattering signals in the present experiments, followed by propane and then methane. However, the extent of increase of the peak scattering in the flickering ethylene flames, relative to the steady flame, is small (25 to 45%) in comparison to the propane flames, which show an enhancement of 75 to 105%. The scattering signals measured in the flickering methane flames are a factor of 30 to 35 larger than the peak signal in the steady flame, dwarfing the scattering enhancements measured for either propane or ethylene. Nevertheless, even the largest scattering signals measured in the flickering methane flames are still

Fig. 10. (See the following page.) Energy-corrected OH· laser-induced fluorescence and soot scattering images in the (A) moderately flickering methane, (B) strongly flickering methane, (C) moderately flickering propane, and (D) moderately flickering ethylene flames, under the same conditions and scalings as in Fig. 9. Ten equally spaced increments in the flicker flame cycle, corresponding to 10-ms intervals, are presented. The 0% phase is arbitrarily set to show the highest development to the right in the figures. Thus, relative to (A), (C) is delayed 10 ms and (B) is delayed 20 ms. The phase lag in the propane flame is presumably a consequence of its lower fuel flow rate.

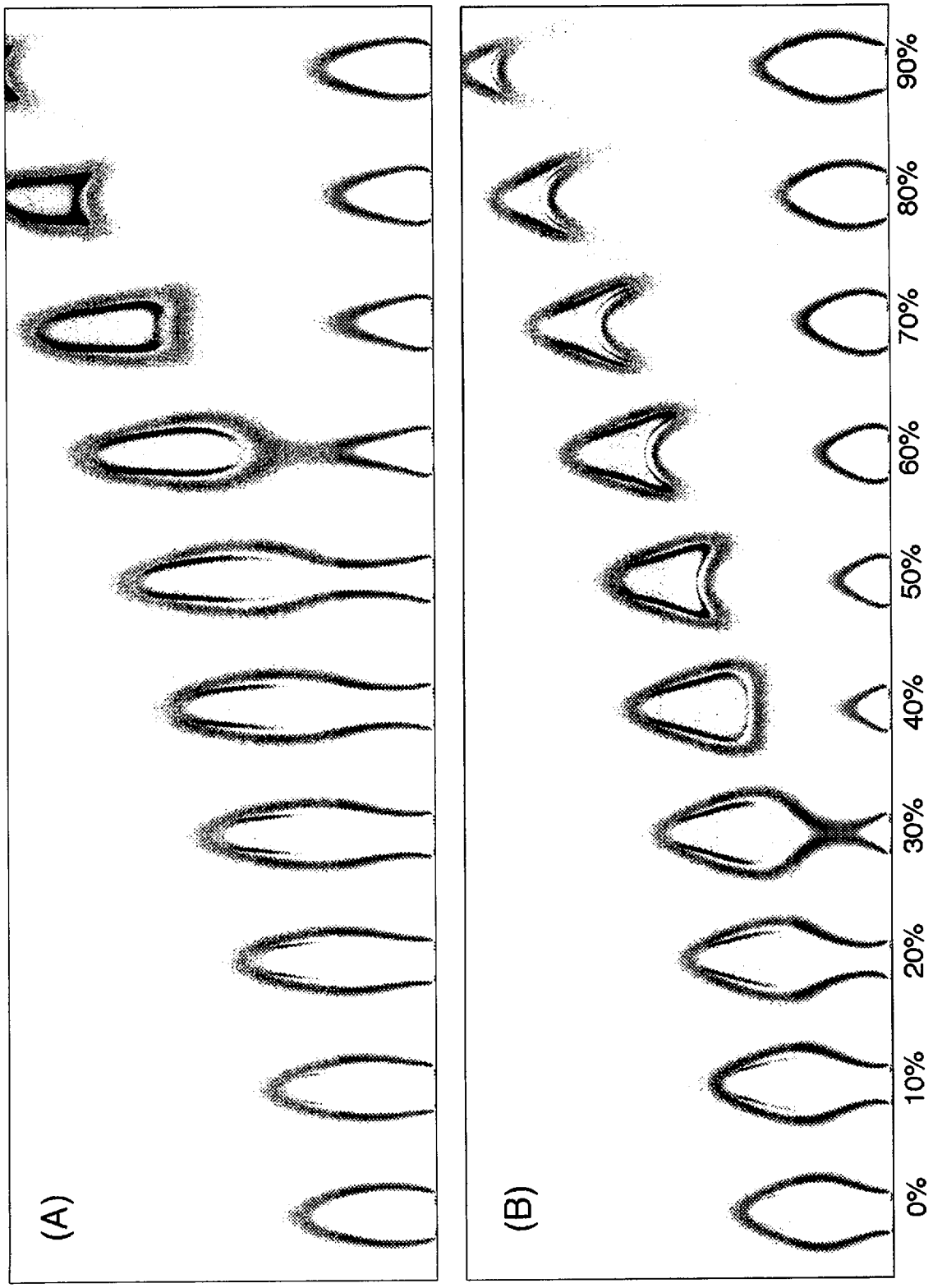
(A)
(B)
0%
10%
20%
30%
40%
50%
60%
70%
80%
90%

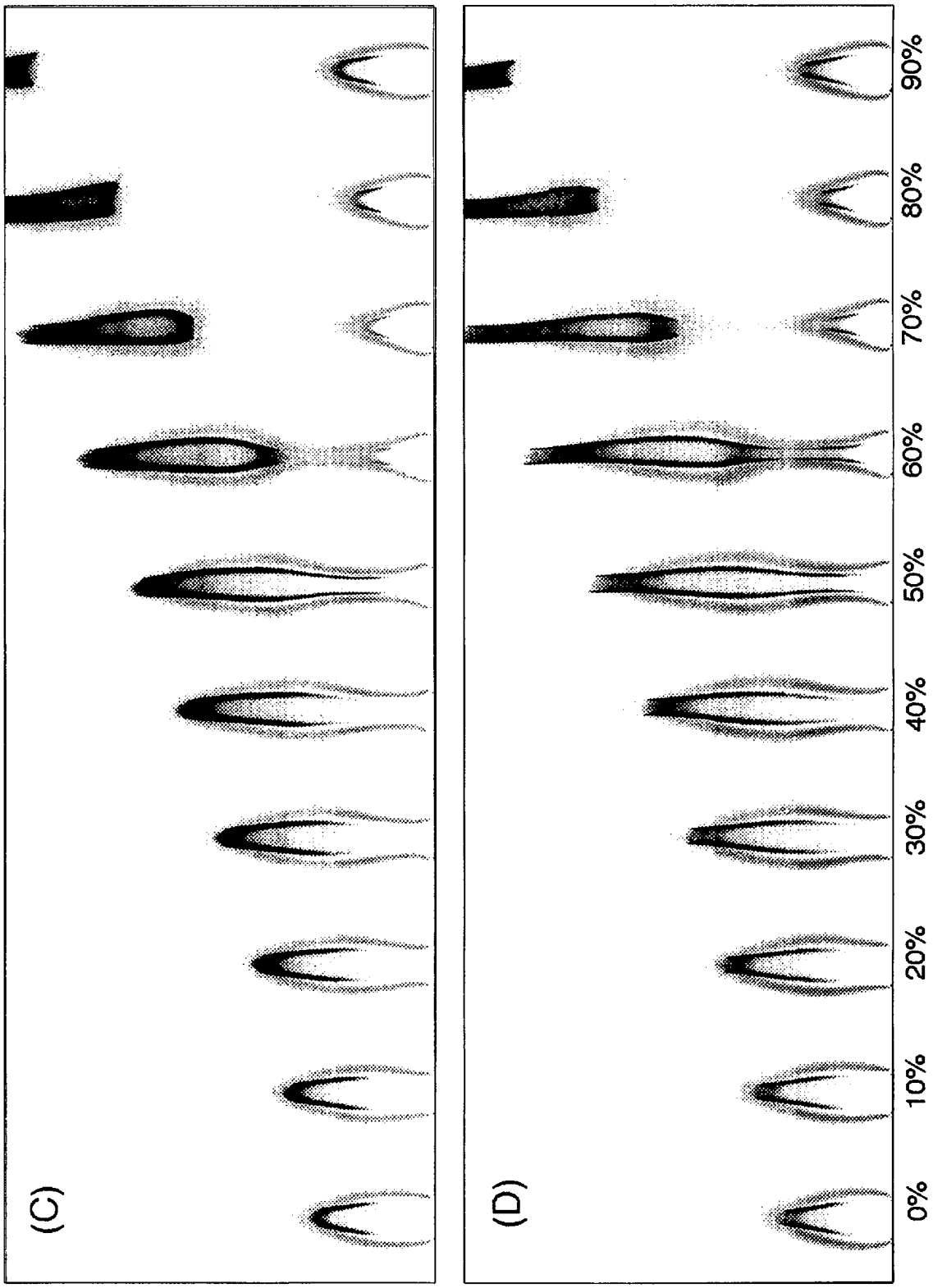
(C)
(D)
0%
10%
20%
30%
40%
50%
60%
70%
80%
90%

substantially lower (3 ×) than the peak scattering level in the steady propane flame. None of these fuels exhibit a significant difference in peak scattering for the two different flicker intensities, and in fact for all cases slightly higher scattering signals are found for the moderately flickering condition.

3.2. Laser-Induced Incandescence

Table 2 also shows the peak, calibrated, corrected LII signals measured for each of the flames. The flickering methane flames were found to exhibit 5.5 to 6 times larger local soot volume fractions than those measured in the steady flame, in close agreement with our earlier LII measurements [14]. In striking contrast, the peak soot levels in the flickering flames of both propane and ethylene are only 35 to 60% higher than the corresponding steady flames. Also, as with the scattering signals, little effect of the flicker intensity is apparent in the peak soot volume fractions. Note that the soot levels in the steady propane flame are much closer to those in the ethylene flame (which are $\approx 2\times$ larger) than those in the methane flame ($\approx 20\times$ smaller).

Soot volume fraction profiles for the three steady flames are shown in Fig. 11. Significant differences in the overall shape of the soot structure are evident as the soot levels increase from the methane flame to the ethylene flame. The soot levels in the methane flame show a distinct region of growth at higher heights toward the center of the flame. In contrast, the propane and, especially, ethylene flames exhibit peak soot concentrations at mid-height in a narrow annular region, with contributions from centerline soot relatively less significant. Similar trends are evident in comparing the soot structures measured in CH_4/air flames with fuel flow rates ranging from 4 to 12 cm^3/s —i.e., the structure of the soot field becomes more annular for higher soot concentrations which occur at the higher flow rates. Honnery and Kent [67] noted the same behavior in C_2H_4/air flames with flow rates ranging from 2 to 44 cm^3/s.

Figure 12A and 12B present the LII line profiles for the two flickering methane flames. Strong growth in the soot volume fraction is evident as the soot field is convected to higher locations during the evolution of the flicker cycle. LII profiles in the moderately flickering propane and ethylene flames are shown as Fig. 12C and 12D. While some increase in local soot volume fraction is evident at higher axial locations, these flames exhibit a much narrower range of soot levels at heights greater than 40 mm. Another difference from the methane flames is the existence of a localized region of enhanced soot volume fraction (and scattering signal) near the bottom of the clipped-off portion of the propane and ethylene flames (evident at 60 to 70% phase of Fig. 12C and 60 to 80% phase of Fig. 12D). Higher local temperatures and radical concentrations may be present in the soot growth region at these locations (inducing rapid soot formation), due to the close proximity of the primary reaction zone. The decreasing width of the flames from methane to propane to ethylene is clearly reflected in the width of the soot profiles. All of these trends are also apparent in examining the LII profiles for the strongly flickering flames.

TABLE 2

Soot Signals in Steady and Flickering Flames

Fuel	Peak Scattering at 560 nm $Q_{vv,90°}$ (10^{-4}/cm · sr)			Peak Soot Volume Fraction f_v (10^{-6})			Integrated Soot Volume Fraction 10^{-8} cm^3		
	Steady flame	Moderately flickering flame	Strongly flickering flame	Steady flame	Moderately flickering flame	Strongly flickering flame	Steady flame	Moderately flickering flame	Strongly flickering flame
Methane	0.69	23.6	23.0	0.33	1.8	2.0	1.2	3.6[a]	4.0
Propane	68	140	120	6.3	10	8.5	14	19[a]	18[a]
Ethylene	160	230	200	13	20	18	31	31[a]	30[a]

[a]These values are lower bounds; see Section 3.2.

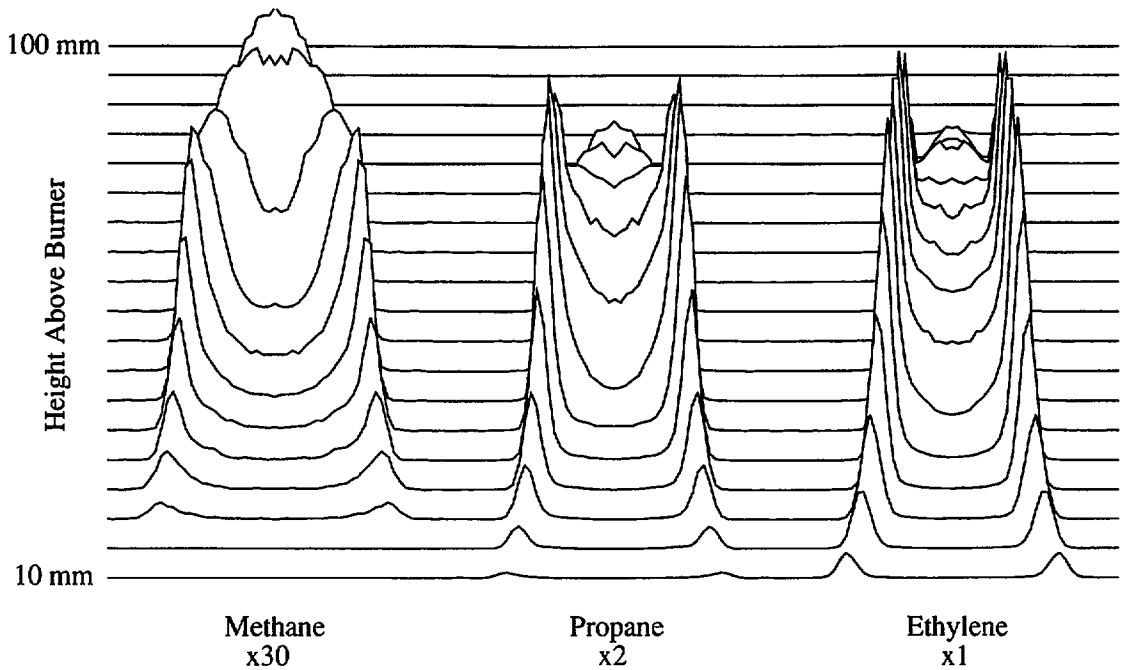

Fig. 11. Overlay profiles of LII-measured soot volume fractions in the steady methane, propane, and ethylene flames, with the indicated relative scalings. The profiles extend from +7 mm to −7 mm radially for each flame and from H = 10 to 100 mm above the burner lip, with 5-mm increments in height. The peak soot volume fraction in the ethylene flame is 13.0 ppm and occurs at a height of 35 mm. All of the profiles shown here have been symmetrized.

In order to compare the overall soot concentrations in the steady and flickering flames, the time-averaged, volume-integrated soot volume fraction was computed from the LII measurements. In this analysis, each radial profile of the local soot volume fraction was first area-integrated, then time-averaged at each height for the ten phase measurements in the flickering flames, and finally integrated over the axial height above the burner. The results of this integration are shown as the final three columns of Table 2. Unfortunately, the experimental set-up restricted the LII imaging to a maximum height of 115 mm above the burner, limiting the domain over which the volume integral could be computed for the flickering flames. In addition, some error is inherent in averaging over the limited temporal and axial sampling, since only ten phase points are considered during the flicker cycle and the axial spacing is 5 mm. The time-averaged, volume-integrated soot volume fraction has been previously analyzed for the steady and moderately flickering CH_4/air flames using extinction measurements spaced 1 ms in time and extending over the entire heights of the flames (in 20-mm axial increments) [14]. This previous analysis showed a factor of 4 enhancement in the moderately flickering flame, in contrast to the factor of 3 increase calculated here. The underestimation due to the measurement height constraint for the strongly flickering

Fig. 12. (See following page.) Overlay profiles of LII-measured soot volume fractions in the (A) moderately flickering methane, (B) strongly flickering methane, (C) moderately flickering propane, and (D) moderately flickering ethylene flames. The methane flame soot volume fractions are scaled up by a factor of 10 relative to the ethylene flame, whereas the propane flame is scaled by a factor of 2. As a point of reference in the ethylene flame, the maximum soot volume fraction is 19.0 ppm at H = 115 mm, 90% phase. The profiles in the moderately flickering flames extend from −11 mm to +11 mm radially for each flame and from H = 10 to 115 mm above the burner lip, with 5-mm increments in height. In the strongly flickering methane flame, the profiles extend from −14 mm to +14 mm radially. The profiles have been symmetrized, except for certain heights at the bottom of the clipped-off flamelets, where the OH· fluorescence and soot scattering images consistently show the same asymmetries which appear in the LII profiles.

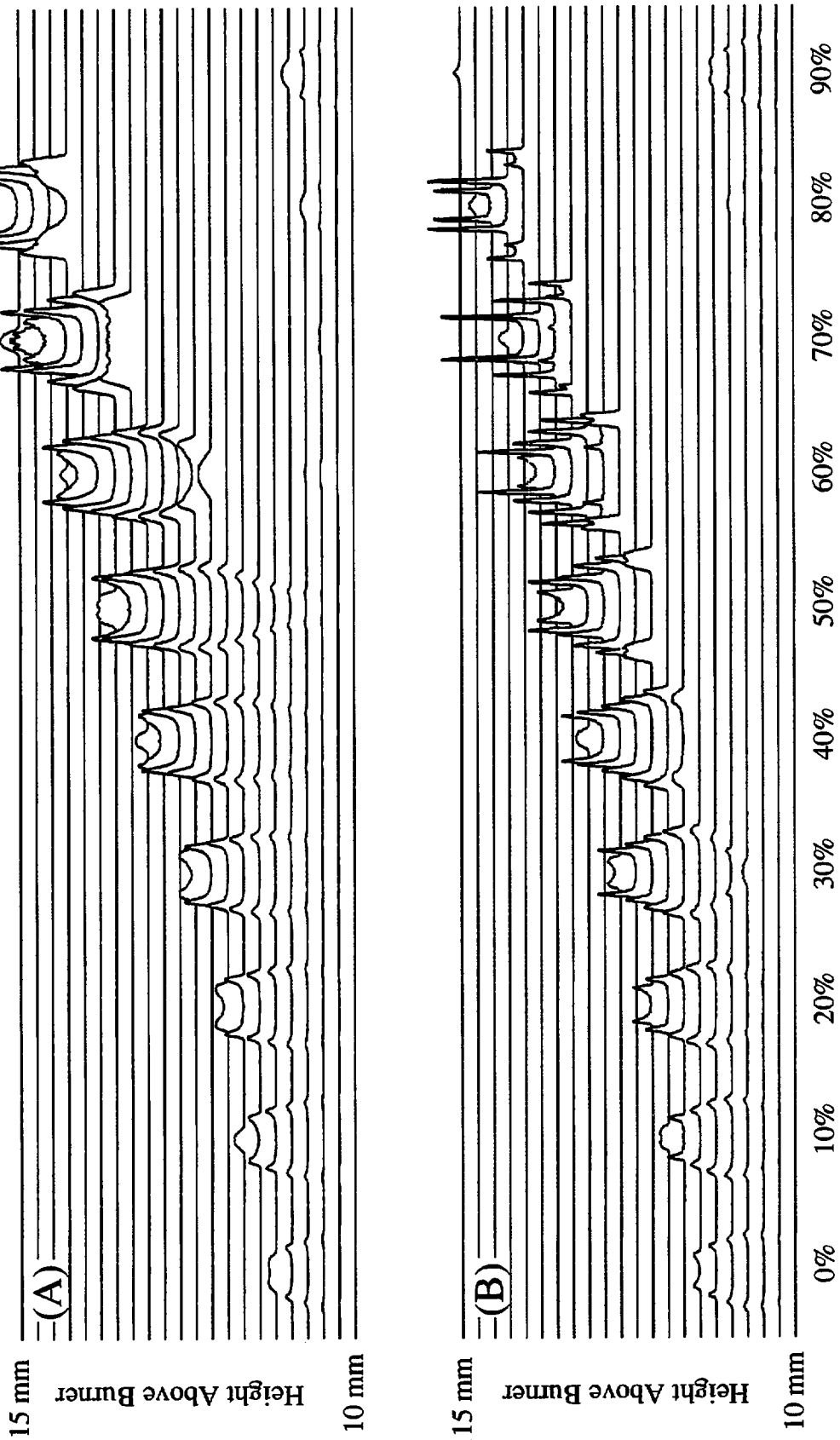
(A)
115 mm
Height Above Burner
10 mm
(B)
115 mm
Height Above Burner
10 mm
0%
10%
20%
30%
40%
50%
60%
70%
80%
90%

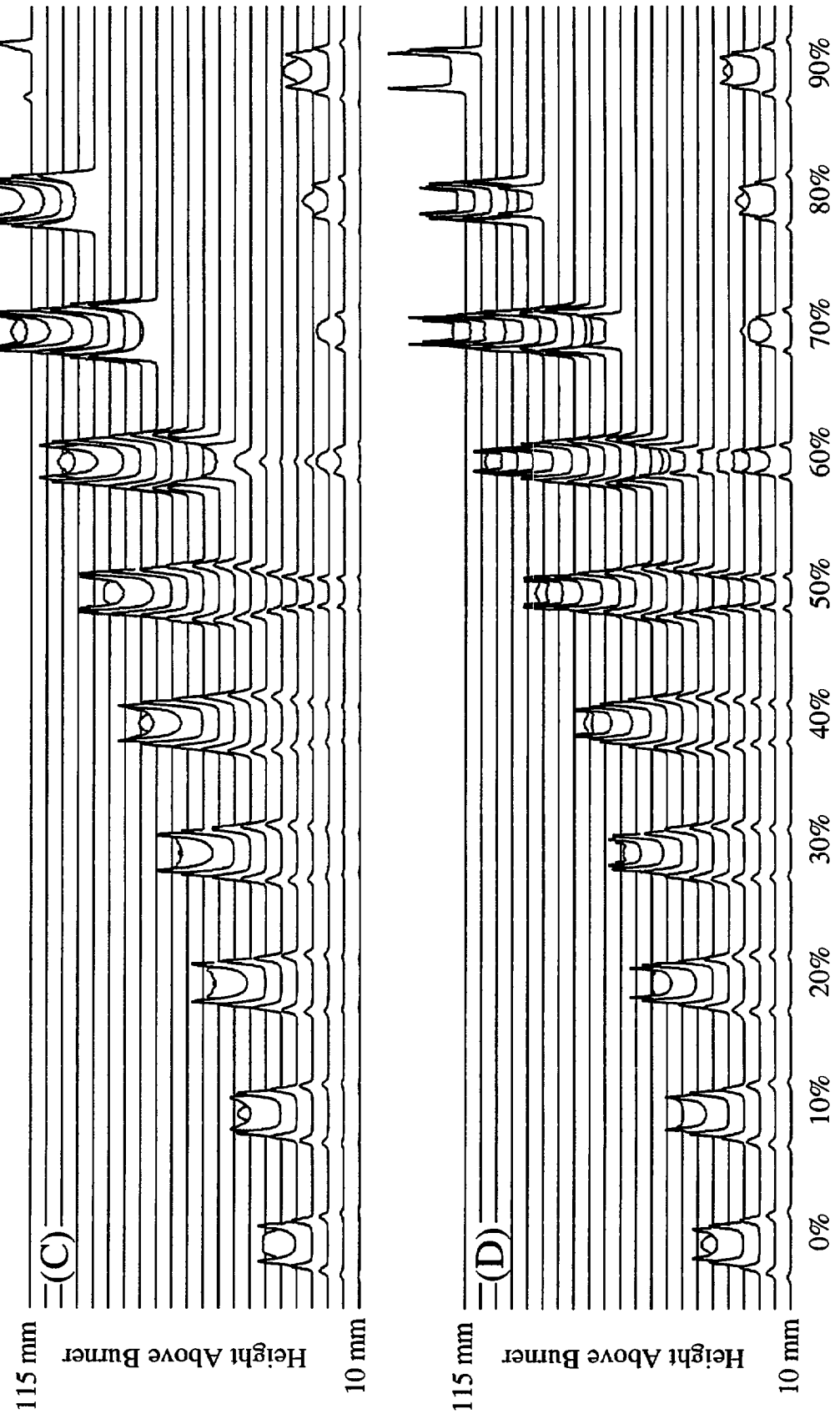
(C)
(D)
Height Above Burner
115 mm
10 mm
0%
10%
20%
30%
40%
50%
60%
70%
80%
90%

methane flame is relatively small, since this flame has a luminous height of $\approx$ 13 cm and the time-averaged, area-integrated soot volume fraction is essentially zero by H = 115 mm. All of the other flickering flames have luminous heights of $\approx$ 17 cm, and thus could show approximately the same extent of underestimation (25%), as is suggested by comparing the LII- and extinction-derived integrations for the moderately flickering methane flame. This computation fails, strictly speaking, for smoking flames (such as the flickering propane and ethylene flames) for which the time-averaged, area-integrated soot volume fraction is always nonzero and extends to infinite heights. For consideration over the active, luminous portion of the soot within the flame, however, this calculation should accurately reflect general trends.

With these considerations in mind, the trends in the integrated soot volume fraction are seen to closely mimic the tendencies of the peak soot volume fraction data. In particular, the flickering methane flames show by far the strongest increase in total soot relative to the steady flame, followed by propane and then ethylene. In fact, the integrated soot concentrations in the ethylene flames are essentially the same for all conditions, though the flickering flame values are lower estimates (as described above). The total soot in the steady ethylene flame is $\approx 2\times$ that in the steady propane flame, which in turn is $\approx 10\times$ that in the steady methane flame.

4. DISCUSSION

In order to aid in understanding both the dramatic enhancement in soot production observed in the flickering methane flames and the much weaker increases evident for propane and ethylene, a Mie analysis was used to estimate soot particle sizes and number densities. For this calculation, the calibrated, corrected, vertically polarized soot scattering measurements were combined with the LII-measured soot volume fraction profiles using a FORTRAN code with the BHMIE subroutine [68]. This analysis quantitatively describes the soot field when the soot particle aggregate size is smaller than a Rayleigh-limit description—i.e., when the Rayleigh-limit and full Mie solutions agree. For the 560.3-nm scattered light used here and an assumed index of refraction of $1.57-0.56i$, the Rayleigh-limit and Mie diameters are essentially identical up to $\approx$ 120-nm particle diameters (at which point the particle size parameter x = 0.67), as is illustrated in Fig. 13. For calculated diameters larger than this, the results of either the Rayleigh-limit or the full Mie solution must be treated with caution. In fact, the Mie solution becomes double-valued for particle sizes on the order of 210 nm. Also shown in Fig. 13 is the rather large effect on the calculated particle sizes (and consequently number densities) which occurs through the use of another widely cited value of the index of refraction, $1.90-0.55i$ [69]. For example, at a scattering-to-volume ratio of 1.5×10^{-4}/nm · sr, use of $1.90-0.55i$ gives a diameter of 100 nm, whereas use of $1.57-0.56i$ yields D = 116 nm.

Since the velocity fields have not been measured in these flames, the time histories of fluid parcels passing through the sooting regions are unknown. Instead, the contour of maximum scattering is used as a rough guide to the time histories of the soot particles in the steady flames, and as an indicator of the general soot field characteristics in the flickering flames. Except at very low heights and near the tops of the flames, the radial peaks of scattering and soot volume fraction are generally coincident (within 0.25 mm). At the tops of the steady flames, where the annular character of the soot field disappears due to oxidation, both the maximum scattering and soot volume fraction signals shift to interior streamlines [34]. However, the annular structure persists in the scattering signals at higher heights and therefore follows the maximum soot streamline longer. At a few heights in the clipped-off portions of the flickering flames, the scattering profiles were found to disagree with the baseline width of the LII-measured soot volume fraction profiles, presumably due to flame wobble during acquisition of the LII and/or scattering signals. In these cases, the scattering profile was radially adjusted (by adding or subtracting points at the centerline) until the edges of the soot volume fraction and scattering coincided.

4.1. Methane Flames

Figure 14 shows the calculated diameters and number densities as a function of height at the radial position of maximum soot scattering for the steady methane flame and for a characteristic short and tall phase of each of the flickering methane flames (see Figs. 10–12). Number densities were calculated assuming a monodisperse size distribution at each measurement location. These values for number density are half those which result from assuming a self-preserving size distribution at each point [18, 70]. As is evident in Fig. 14, the maximum soot particle size in the steady methane flame is just over 60 nm, in excellent agreement with our previous analysis of the UV scattering and LII data [14] and the determination by Richardson and Santoro [66]. For early, short phases of the flickering flames (e.g., 20% in Fig. 10), the peak particle sizes are somewhat larger ($\approx$ 80 nm), whereas for later clipped-off phases the particle sizes approach 110 nm. In the moderately flickering methane flame, significant particle size growth is evident in the clipped-off segment as a function of height. In contrast, in the strongly flickering flame the particle sizes appear to reach a plateau except in the soot oxidation regions at the top and bottom of the burning flamelet. Another feature evident in Fig. 14 (top) is the sharper particle-size fall-offs at the tops of the flickering flames (at any phase) relative to the corresponding steady flames. One cause of this effect could be a slower centerline soot formation rate relative to the annular layer soot in the flickering flames, similar to the effect seen in steady flames with higher fuel flow rates or with fuels of higher sooting tendency. A second possible explanation is the likely straining of the flame structure at the top of the flickering flame due to the buoyant acceleration of combusting fuel gases into relatively cool and stagnant air brought to the centerline through the action of the external vortex rings.

The number densities in the methane flame, Fig. 14 (bottom), generally show a decline with increasing height, presumably due to the effect of particle agglomeration. As the position of

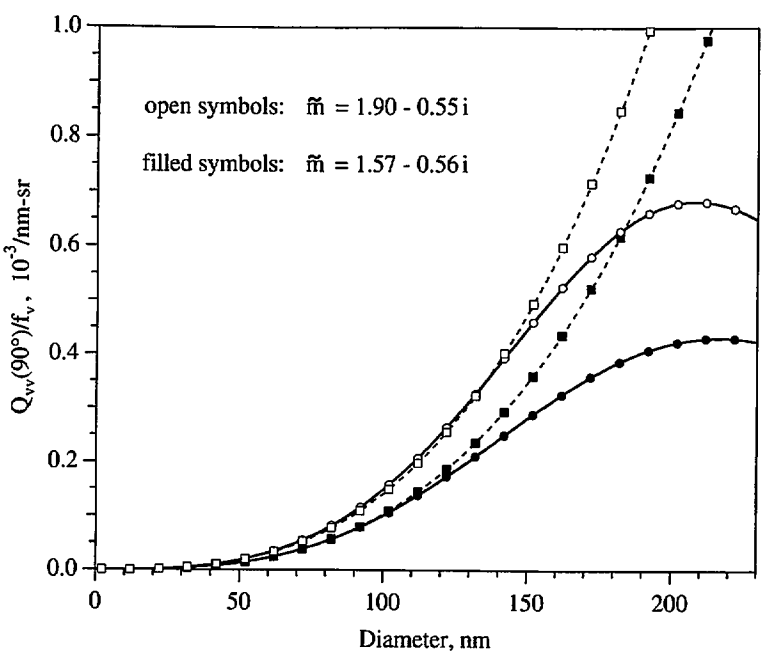

Fig. 13. Calculated ratio of the vertically polarized scattering cross section at 90° to the soot volume fraction as a function of soot particle size diameter for a monodisperse size distribution. Both the Rayleigh-limit solution (□, ■; dashed lines) and the full Mie theory solution (○, ●; solid lines) are shown for two commonly employed values of the soot index of refraction. The abscissa represents the measured input parameter used to solve for the particle diameters in the Rayleigh-limit and Mie analyses of the flame data.

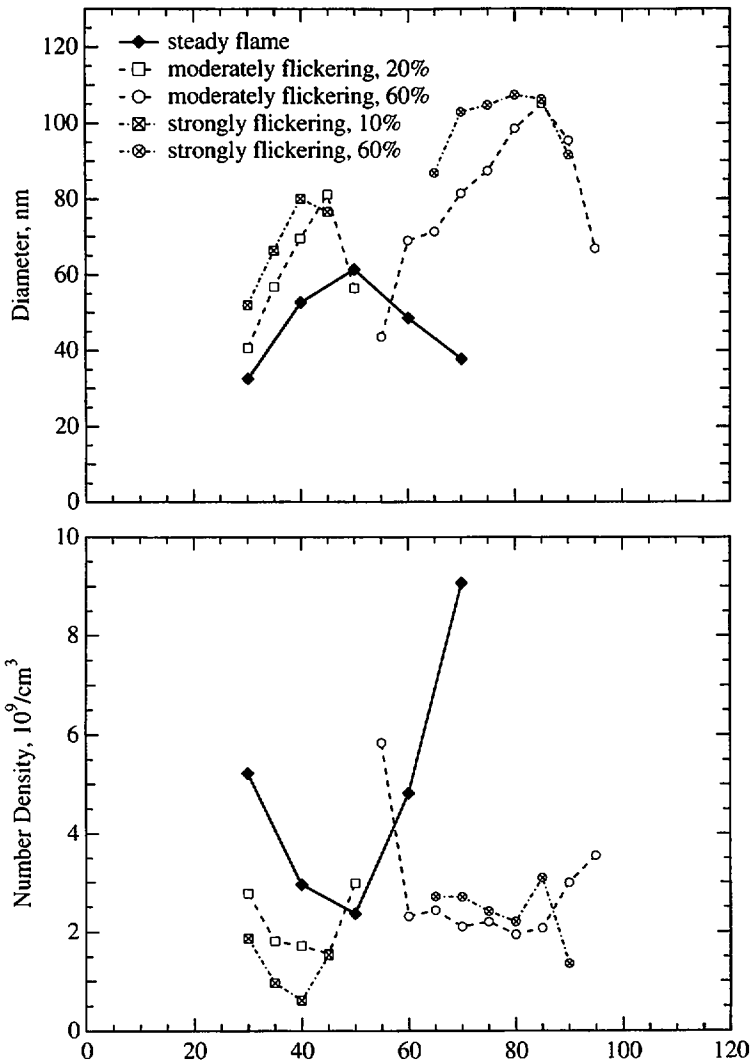

Fig. 14. Calculated Mie theory diameters (top) and number densities (bottom) for the indicated CH_4/air flame conditions as a function of axial height above the burner lip. The flickering flame phase designations refer to the phase identification in Fig. 10.

maximum soot scattering moves to interior regions near the tops of the flames, the number density shows a sharp rise, particularly for the steady flame. Mie calculations across the full radial soot profiles also exhibit a rapid increase in particle number density with increasing height near the centerline as the top of the flame is approached, indicating that significant particle inception is occurring in these regions. At early development times in the flickering flames, the number density at the location of the peak particle size can be a factor of 4 lower than the corresponding number density in the steady flame, suggesting that the larger particles found in this region arise predominantly from an increased extent of agglomeration relative to the steady flame. In contrast, the number densities in the clipped-off portions of the flickering flames generally remain greater than $2 \times 10^9/cm^3$, close to the number density corresponding to the largest soot particles in the steady flame. This result shows that the much

larger soot particles present in the higher portions of the flickering methane flames are due primarily to increased soot mass growth.

4.2. Propane Flames

The Mie results for the propane flames are presented in Fig. 15. Here, the peak diameter in the steady flame is significantly larger than for methane, $D \approx 105$ nm. In the early time development of the flickering flames, the peak diameter is slightly higher (≈ 110 nm) than in the steady flame, and in the clipped-off portions, the soot particles reach diameters of 120 nm. The trends in particle diameters closely parallel those found for the methane flames, except, as was the case in comparing soot volume fractions, the propane flames show a much reduced relative growth effect. The number density contours also show trends similar to the methane data, namely, the number densities for the early times in the flickering flames

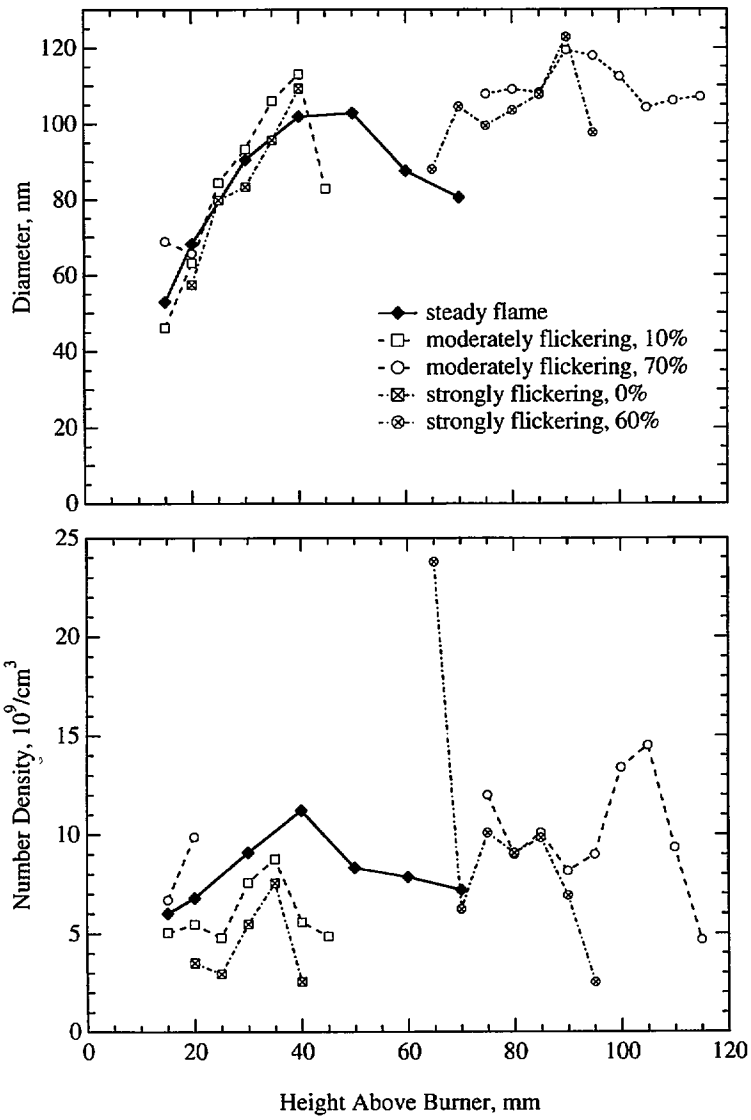

Fig. 15. Calculated Mie theory diameters (top) and number densities (bottom) for the indicated C_3H_8/air flame conditions as a function of axial height above the burner lip. The phase designations for the moderately flickering flame refer to the phase identification in Fig. 10.

are lower than those of the steady flame (though by less than a factor of two), whereas the clipped-off portions exhibit comparable number densities. In contrast to the methane flames, as the contour of maximum scattering moves to interior regions at the tops of the propane flames the number densities decline markedly, suggesting a relatively reduced degree of particle inception near the centerline. The very high number density present at the base of the clipped-off section of the strongly flickering flame suggests that soot inception is vigorous at this location. It should be noted, however, that even a small discrepancy in the effective measurement location between the LII and scattering data could lead to significant differences in the Mie calculation at this location, where axial gradients are large. Note that the propane flame number densities are $\approx 4 \times$ greater than those found in the methane flames.

4.3. Ethylene Flames

Figure 16 shows that the peak soot diameter in the steady ethylene flame is approximately 110

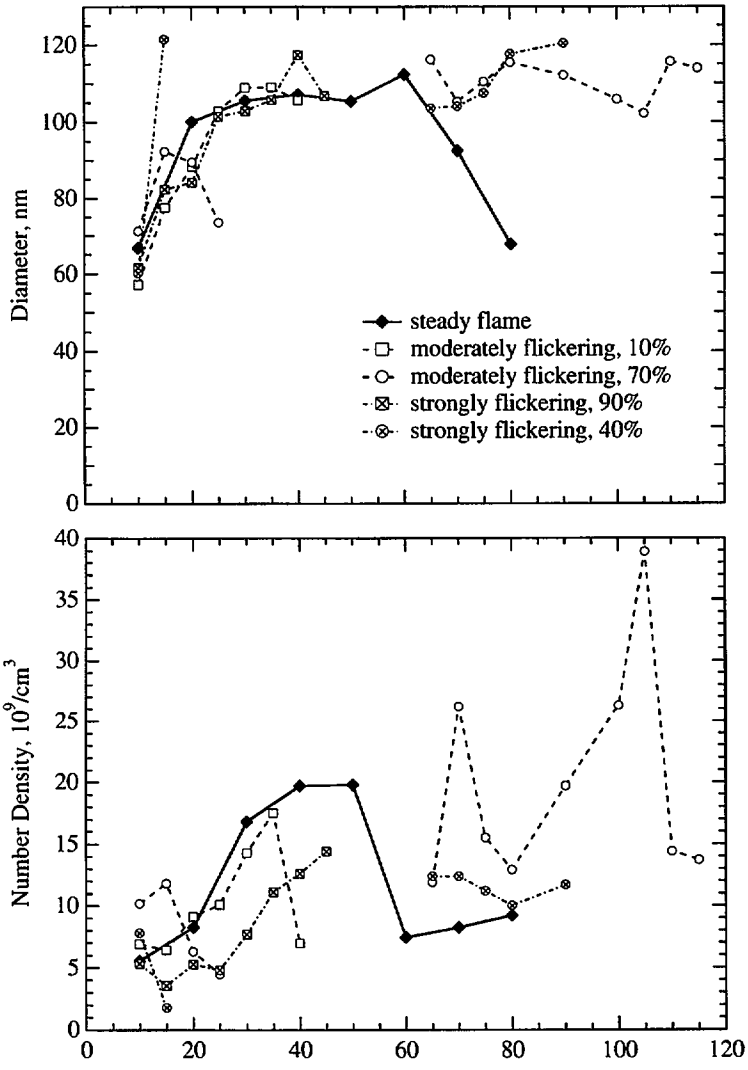

Fig. 16. Calculated Mie theory diameters (top) and number densities (bottom) for the indicated C_2H_4/air flame conditions as a function of axial height above the burner lip. The phase designations for the moderately flickering flame refer to the phase identification in Fig. 10.

nm, and little growth in the soot particle size occurs from approximately 20 mm in height until the soot is oxidized. Similarly, the peak sizes in both the early development and the clipped-off portions of the flickering flames are generally near 110 nm, with an occasional point calculated to have a diameter of 120 nm. As with the propane analysis, the number densities generally rise through the annular soot growth region and then fall as the peak scattering moves to more interior streamlines. The number densities in the early development of the flickering flames are somewhat smaller than for the steady flame. This is also true for the clipped-off portions of the strongly flickering flame.

4.4. Relative Soot Enhancement in the Flickering Flames

Two general hypotheses can be considered to explain the observed differences in relative soot production between flickering and steady flames of methane, propane, and ethylene. First, the characteristic residence times available for soot formation and growth in the flickering flames may differ markedly between methane and the other fuels, due to differences in radiative heat loss, thermal expansion, and the resulting vortical structure intensity. Unfortunately, this hypothesis cannot be addressed experimentally until time-resolved, full-field velocity and temperature measurements are made in these flames. This hypothesis is not particularly convincing, since the flickering propane and ethylene flames exhibit appreciably larger luminous flame heights than the corresponding steady flames ($\approx$ 17 cm vs. $\approx$ 9 cm), suggesting significantly longer residence times. In theory, simulations of the steady and flickering flames for the different fuels which accurately predict flame structure evolution and local soot concentrations could be used to generate information about the time history of the fluid parcels which pass through the maximum sooting regions. However, such computations have thus far been performed only for the methane-fueled flames, where residence times were estimated to increase by a factor of 2 [15].

A second possible explanation for the observed soot production behavior is that the ability of propane and ethylene fuels to utilize the additional residence time for soot mass growth in the flickering flames is limited, due to a loss in soot particle reactivity or depletion of growth species. Whereas a recent detailed study of soot formation in a weakly buoyant acetylene/air diffusion flame found no evidence for significant aging effects on soot reactivity [71], some support exists in the literature for the hypothesis that depletion of growth species plays a role in reduced soot growth rates for propane and, especially, ethylene. Rapp and Santoro [72] have found that the concentrations of acetylene and other potential soot-growth hydrocarbons collapse at the location of the maximum soot volume fraction in their Non-Smoking steady ethylene flame, suggesting that this depletion is the cause for cessation of soot mass growth. The observed decline of relative soot production rates along the centerline for heavily sooting flames may be understood in terms of this effect, since soot formation and growth along the centerline necessarily occur at higher axial locations, where the intermediate hydrocarbon levels have started to fall. Similarly, Honnery and Kent [67] have found that, for ethylene flow rates substantially larger than 2 cm^3/s, the maximum fraction of fuel carbon converted to soot remains approximately constant at 20%. This result seems to imply that there exists a fundamental limitation for a given fuel in its ability to convert fuel carbon to soot, which is presumably manifested through a limited capability to convert the hydrocarbon fuel to the appropriate soot growth species. Lindstedt [27] has reported that his modeling of soot formation in propane and ethylene counterflow diffusion flames best fits experimental data under the assumption that the soot surface growth rate is independent of the surface area and only depends on the number of particles. Moss and co-workers have also found that the surface growth rate is independent of surface area for ethylene diffusion flames [9, 22], but not for methane/air flames [16], resulting in a much stronger residence time effect for the methane/air system. Thus, it appears that, for the sizes of steady flames considered here, the methane system is still far from its limit of

conversion to soot, whereas propane and ethylene are much closer to their respective limits.

Irrespective of the degree of enhancement in soot concentrations, flickering flames provide a longer residence time for the soot to radiate energy away from the flame, resulting in cooler flame temperatures near the flame apex. For the propane and ethylene flow rates and flicker intensities investigated here, the increased heat loss from the flickering flames results in soot breakout during a portion of the flicker cycle. Even though the flickering methane flame exhibits the largest extent of enhancement in local soot concentration and probably also experiences the largest increase in soot residence time in the flame, the soot loading in this flame is too small to result in smoke emission for our experimental conditions.

5. CONCLUSIONS

Previous studies of soot production in a steady and moderately flickering methane/air diffusion flame with the same mean fuel flow rate have been expanded to include steady and flickering propane/air and ethylene/air flames. Soot volume fraction profiles have been quantitatively measured using laser-induced incandescence, calibrated to laser-extinction measurements in a steady CH_4/air flame. This calibration has been found to be accurate over soot volume fractions ranging from 0.05 to 10 ppm, optically derived soot particle sizes from 30 to 115 nm, and number densities from 2×10^9 to 2×10^{10} cm^{-3}. The laser-induced incandescence technique has been developed to better quantify temporally and spatially resolved soot volume fractions through the use of an improved choice of detector bandpass and corrections for the effects of laser focus/spatial averaging and in-flame extinction of the LII signal. The phase-resolved soot volume fraction measurements in the flickering flames constitute a useful database for testing several recently formulated integrated soot models in a complex, time-varying environment. Calibrated, vertically polarized soot scattering measurements at 560.3 nm have also been obtained in these flames and have been corrected for soot extinction effects. Finally, laser-induced fluorescence from laser-produced C_2 was examined as a possible measure of soot volume fraction [48, 49]. However, the C_2 LIF signal does not track the local soot volume fraction for concentrations above 2 ppm at the laser intensities used in our experiments.

The peak soot scattering and soot volume fractions in flickering CH_4/air flames are greatly enhanced relative to the steady flame values. In contrast, the scattering signals and volume fractions in the flickering propane/air and ethylene/air flames are only moderately enhanced relative to the corresponding steady flames, yet these flickering flames emit smoke. Time-averaged, volume-integrated soot volume fractions show that the same trends evident in comparing the peak soot volume fractions for the different flames also hold for the integrated soot concentrations. No significant effect of flicker intensity is evident for any of these soot field measurements.

Mie analysis of the scattering and soot volume fraction data shows that the peak soot particle diameters reach 110 nm in the flickering methane flames compared to 60 nm in the steady flame, while the particle number densities at these locations remain similar. Peak particle sizes increase from 105 nm in the steady propane flame to approximately 120 nm in the propane flickering flames and from 110 nm in the steady ethylene flame to approximately 120 nm in the ethylene flickering flames. The dramatic differences in soot production between flickering methane flames and flickering flames of propane and ethylene appear to be consistent with the concept that a fundamental limit exists for the ability of fuel carbon to be converted to soot in a diffusion flame of a given hydrocarbon fuel. This effect is manifested through a limited supply of the appropriate soot growth species. For the flow rates and burner geometry of the present experiments, the steady methane flame is far from its maximum soot production, whereas the steady propane flame is relatively near its limit and the steady ethylene flame is quite close to its limit. The observed emission of smoke from the flickering propane and ethylene flames demonstrates the influence of radiative cooling

on soot oxidation and breakout in time-varying flames.

The authors gratefully acknowledge significant support of this work by the Basic Sciences Group, Gas Research Institute under Contract No. 5093-260-2676. David A. Everest capably assisted in the measurements of LII fluence dependence and C_2 fluorescence, and John Hagerdorn provided expertise in imaging and plotting software.

REFERENCES

1. Hamins, A., Yang, J. C., and Kashiwagi, T., *Twenty-Fourth Symposium (International) on Combustion*, The Combustion Institute, Pittsburgh, 1992, pp. 1695–1702.
2. Cetegen, B. M., and Ahmed, T. A., *Combust. Flame* 93:157–184 (1993).
3. Buckmaster, J., and Peters, N., *Twenty-First Symposium (International) on Combustion*, The Combustion Institute, Pittsburgh, 1986, pp. 1829–1836.
4. Ellzey, J. L., and Oran, E. S., *Twenty-Third Symposium (International) on Combustion*, The Combustion Institute, Pittsburgh, 1990, pp. 1635–1640.
5. Davis, R. W., Moore, E. F., Roquemore, W. M., Chen, L.-D., Vilimpoc, V., and Goss, L. P., *Combust. Flame* 83:263–270 (1991).
6. Smyth, K. C., Miller, J. H., Dorfman, R. C., Mallard, W. G., and Santoro, R. J., *Combust. Flame* 62:157–181 (1985).
7. Kent, J. H., and Honnery, D., *Combust. Sci. Technol.* 54:383–397 (1987).
8. Kent, J. H., and Honnery, D. R., *Combust. Flame* 79:287–298 (1990).
9. Moss, J. B., Stewart, C. D., and Syed, K. J., *Twenty-Second Symposium (International) on Combustion*, The Combustion Institute, Pittsburgh, 1988, pp. 413–423.
10. Sivathanu, Y. R., and Gore, J. P., Central and Eastern States Meeting of the Combustion Institute (New Orleans, March 1993), paper #123.
11. Puri, R., Santoro, R. J., and Smyth, K. C., *Combust. Flame* 97:125–144 (1994) and Erratum, *Combust. Flame* 102:226–228 (1995).
12. Kent, J. H., and Wagner, H. Gg., *Combust. Sci. Technol.* 41:245–269 (1984).
13. Smyth, K. C., Harrington, J. E., Johnsson, E. L., and Pitts, W. M., *Combust. Flame* 95:229–239 (1993).
14. Shaddix, C. R., Harrington, J. E., and Smyth, K. C., *Combust. Flame* 99:723–732 (1994).
15. Kaplan, C. R., Shaddix, C. R., and Smyth, K. C., *Combust. Flame*, 106:392–405 (1996).
16. Syed, K. J., Stewart, C. D., and Moss, J. B., *Twenty-Third Symposium (International) on Combustion*, The Combustion Institute, Pittsburgh, 1990, pp. 1533–1541.
17. Kent, J. H., Jander, H., and Wagner, H. Gg., *Eighteenth Symposium (International) on Combustion*, The Combustion Institute, Pittsburgh, 1981, pp. 1117–1126.
18. Santoro, R. J., Semerjian, H. G., and Dobbins, R. A., *Combust. Flame* 51:203–218 (1983).
19. Vandsburger, U., Kennedy, I., and Glassman, I., *Combust. Sci. Technol.* 39:263–285 (1984).
20. Glassman, I., *Twenty-Second Symposium (International) on Combustion*, The Combustion Institute, Pittsburgh, 1988, pp. 295–311, and references therein.
21. Stewart, C. D., Syed, K. J., and Moss, J. B., *Combust. Sci. Technol.* 75:211–226 (1991).
22. Moss, J. B., Stewart, C. D., and Young, K. J., *Combust. Flame* 101:491–500 (1995).
23. Kennedy, I. M., Kollmann, W., and Chen, J.-Y., *Combust. Flame* 81:73–85 (1990).
24. Kennedy, I. M., Kollmann, W., and Chen, J.-Y., *AIAA J.* 29:1452–1457 (1991).
25. Villasenor, R., and Kennedy, I. M., *Twenty-Fourth Symposium (International) on Combustion*, The Combustion Institute, Pittsburgh, 1992, pp. 1023–1030.
26. Leung, K. M., Lindstedt, R. P., and Jones, W. P., *Combust. Flame* 87:289–305 (1991).
27. Lindstedt, R. P., *Soot Formation in Combustion: Mechanisms and Models*, Springer-Verlag Series in Chemical Physics 59 (H. Bockhorn, Ed.), pp. 417–441 (1994).
28. Honnery, D. R., and Kent, J. H., *Twenty-Fourth Symposium (International) on Combustion*, The Combustion Institute, Pittsburgh, 1992, pp. 1041–1047.
29. Honnery, D. R., Tappe, M., and Kent, J. H., *Combust. Sci. Technol.* 83:305–321 (1992).
30. Kent, J. H., and Honnery, D. R., *Soot Formation in Combustion: Mechanisms and Models*, Springer-Verlag Series in Chemical Physics 59 (H. Bockhorn, Ed.), pp. 199–220 (1994).
31. Dobbins, R. A., and Megaridis, C. M., *Appl. Opt.* 30:4747–4754 (1991).
32. Charalampopoulos, T. T., and Chang, H., *Combust. Flame* 87:89–99 (1991).
33. Puri, R., Moser, M., Santoro, R. J., and Smyth, K. C., *Twenty-Fourth Symposium (International) on Combustion*, The Combustion Institute, Pittsburgh, 1992, pp. 1015–1022.
34. Santoro, R. J., Yeh, T. T., Horvath, J. J., and Semerjian, H. G., *Combust. Sci. Technol.* 53:89–115 (1987).
35. Megaridis, C. M., and Dobbins, R. A., *Twenty-Second Symposium (International) on Combustion*, The Combustion Institute, Pittsburgh, 1988, pp. 353–362.
36. Puri, R., Richardson, T. F., Santoro, R. J., and Dobbins, R. A., *Combust. Flame* 92:320–333 (1993).
37. Miller, J. H., Mallard, W. G., and Smyth, K. C., *Combust. Flame* 47:205–214 (1982) and unpublished results from this laboratory.
38. Landolt-Börnstein, *Zahlenwerte und Funktionen aus Physik, Chemie, Astronomie, Geophysik, und Technik*, II. Band, 8. Teil, *Optische Konstanten*. Springer-Verlag, Berlin, 1962.

39. Bogaard, M. P., Buckingham, A. D., Pierens, R. K., and White, A. H., *J. Chem. Soc., Faraday Trans. I* 74:3008–3015 (1978).
40. Bridge, N. J., and Buckingham, A. D., *Proc. Royal Soc., A* 295:334–349 (1966).
41. Dalzell, W. H., and Sarofim, A. F., *J. Heat Transfer* 91:100–104 (1969).
42. Smyth, K. C., and Shaddix, C. R., *Combust. Flame*, in press.
43. Dasch, C. J., *Appl. Opt.* 31:1146–1152 (1992), and associated computer spreadsheet program.
44. Leider, H. R., Krikorian, O. H., and Young, D. A., *Carbon* 11:555–563 (1973).
45. Eckbreth, A. C., *J. Appl. Phys.* 48:4473–4479 (1977).
46. Melton, L. A., *Appl. Opt.* 23:2201–2208 (1984).
47. Quay, B., Lee, T.-W., Ni, T., and Santoro, R. J., *Combust. Flame* 97:384–392 (1994).
48. Bengtsson, P.-E., and Aldén, M., *Combust. Sci. Technol.* 77:307–318 (1991).
49. Bengtsson, P.-E., and Aldén, M., *Appl. Phys. B* 60:51–59 (1995).
50. Huber, K. P., and Herzberg, G., *Molecular Spectra and Molecular Structure, IV. Constants of Diatomic Molecules*, Van Nostrand Reinhold, New York, 1979.
51. Tyte, D. C., Innanen, S. H., and Nicholls, R. W., *Identification Atlas of Molecular Structure, 5. The C_2 $A^3\Pi_g$—$X'^3\Pi_u$ Swan System*, York University, England, 1967.
52. Bengtsson, P.-E., and Aldén, M., *Combust. Flame* 80:322–328 (1990).
53. Dec, J. E., zur Loye, A. O., and Siebers, D. L., *SAE Technical Papers Series* SAE-910224, Society of Automotive Engineers, PA, 1991.
54. Black, J. G., Yablonovitch, E., Bloembergen, N., and Mukamel, S., *Phys. Rev. Lett.* 38:1131–1134 (1977).
55. Dasch, C. J., *Appl. Opt.* 23:2209–2215 (1984).
56. Eckbreth, A. C., in *Experimental Diagnostics in Gas Phase Combustion Systems* (B. T. Zinn, Ed.), AIAA, New York, 1977, pp. 517–547.
57. Tait, N. P., and Greenhalgh, D. A., *Ber. Bunsenges. Phys. Chem.* 97:1619–1625 (1993).
58. Hofeldt, D. L., *SAE Technical Papers Series* SAE-930079, Society of Automotive Engineers, PA, 1993.
59. Ni, T., Pinson, J. A., Gupta, S., and Santoro, R. J., *Appl. Opt.* 34:7083–7091 (1995).
60. Vander Wal, R. L., and Weiland, K. J., *Appl. Phys. B* 59:445–452 (1994).
61. Case, M. E., Hofeldt, D. L., and Kittelson, D. B., Central States Meeting of the Combustion Institute, Madison, WI, June 1994, pp. 299–304.
62. Vander Wal, R. L., personal communication (August 1995).
63. Cignoli, F., Benecchi, S., and Zizak, G., *Appl. Opt.* 33:5778–5782 (1994).
64. Megaridis, C. M., and Dobbins, R. A., *Combust. Sci. Technol.* 66:1–16 (1989).
65. Megaridis, C. M., personal communication (March 1996) from J. Zhang, Ph.D. thesis, Mechanical Engineering Department, University of Illinois at Chicago, 1996.
66. Richardson, T. F., and Santoro, R. J., personal communication (March 1993).
67. Honnery, D. R., and Kent, J. H., *Combust. Flame* 82:426–434 (1990).
68. Bohren, C. F., and Huffman, D. R., *Absorption and Scattering of Light by Small Particles*, Wiley, New York, 1983, pp. 477–482.
69. Lee, S. C., and Tien, C. L., *Eighteenth Symposium (International) on Combustion*, The Combustion Institute, Pittsburgh, 1981, pp. 1159–1166.
70. Graham, S. C., and Robinson, A., *J. Aerosol Sci.* 7:261–273 (1976).
71. Sunderland, P. B., Köylü, Ü. Ö., and Faeth, G. M., *Combust. Flame* 100:310–322 (1995).
72. Rapp, D. C., and Santoro, R. J., Western States Meeting of the Combustion Institute, Davis CA, March 1994, paper #52.

Received 15 September 1995; revised 9 April 1996